



Original Paper

A seismic elastic moduli module for the measurements of low-frequency wave dispersion and attenuation of fluid-saturated rocks under different pressures



Yan-Xiao He ^a, Shang-Xu Wang ^{a,*}, Gen-Yang Tang ^a, Chao Sun ^b, Hong-Bing Li ^{c,**},
San-Yi Yuan ^a, Xian Wei ^d, Li-Deng Gan ^c, Xiao-Feng Dai ^c, Qiang Ge ^c, Peng-Peng Wei ^e,
Hui-Qing Zhang ^e

^a National Key Laboratory of Petroleum Resources and Engineering, CNPC Key Lab of Geophysical Exploration, College of Geophysics, China University of Petroleum (Beijing), Beijing, 102249, China

^b School of Resources and Geosciences, China University of Mining and Technology, Xuzhou, 221116, Jiangsu, China

^c Research Institute of Petroleum Exploration and Development, CNPC, Beijing, 100083, China

^d Beijing Vocational College of Labour and Social Security, Beijing, 100029, China

^e PetroChina Dagang Oilfield Exploration and Development Research Institute, CNPC, Tianjin, 300280, China

ARTICLE INFO

Article history:

Received 14 November 2022

Received in revised form

2 April 2023

Accepted 30 August 2023

Available online 1 September 2023

Edited by Jie Hao and Meng-Jiao Zhou

Keywords:

Low-frequency measurements

Dispersion and attenuation

Rock physics

Fluid flow

ABSTRACT

Knowledge about the seismic elastic modulus dispersion, and associated attenuation, in fluid-saturated rocks is essential for better interpretation of seismic observations taken as part of hydrocarbon identification and time-lapse seismic surveillance of both conventional and unconventional reservoir and overburden performances. A Seismic Elastic Moduli Module has been developed, based on the forced-oscillations method, to experimentally investigate the frequency dependence of Young's modulus and Poisson's ratio, as well as the inferred attenuation, of cylindrical samples under different confining pressure conditions. Calibration with three standard samples showed that the measured elastic moduli were consistent with the published data, indicating that the new apparatus can operate reliably over a wide frequency range of $f \in [1-2000, 10^6]$ Hz. The Young's modulus and Poisson's ratio of the shale and the tight sandstone samples were measured under axial stress oscillations to assess the frequency- and pressure-dependent effects. Under dry condition, both samples appear to be nearly frequency independent, with weak pressure dependence for the shale and significant pressure dependence for the sandstone. In particular, it was found that the tight sandstone with complex pore microstructure exhibited apparent dispersion and attenuation under brine or glycerin saturation conditions, the levels of which were strongly influenced by the increased effective pressure. In addition, the measured Young's moduli results were compared with the theoretical predictions from a scaled poroelastic model with a reasonably good agreement, revealing that the combined fluid flow mechanisms at both mesoscopic and microscopic scales possibly responsible for the measured dispersion.

© 2024 The Authors. Publishing services by Elsevier B.V. on behalf of KeAi Communications Co. Ltd. This is an open access article under the CC BY-NC-ND license (<http://creativecommons.org/licenses/by-nc-nd/4.0/>).

1. Introduction

Attenuation and dispersion of seismic waves in poroelastic sedimentary rocks saturated by fluids are of significant interest as it

has been recently reported that unconventional hydrocarbon reservoirs have often shown high attenuation and dispersion over a broad range of frequencies and scales (e.g., Chapman et al., 2019). Seismic attenuation, defined here as the inverse quality factor ($1/Q$), corresponds to the mechanical energy absorption of wave amplitudes with distance, whereas dispersion refers to the variations of elastic behavior with frequency. In the absence of scattering or inertial effects, the frequency dependence of elastic properties in fluid-saturated rocks is thought to mainly stem from the physical

* Corresponding author.

** Corresponding author.

E-mail addresses: wangsx@cup.edu.cn (S.-X. Wang), hbingli@petrochina.com.cn (H.-B. Li).

mechanism widely known as the wave-induced fluid flows (WIFFs) caused by the fluid pressure diffusion in the rocks' porous space due to a passing wave. A direct comparison of rocks' elastic properties inferred from the laboratory ultrasonic (i.e., ~MHz) measurements with those at intermediate to low frequencies, such as those utilized in the field (i.e., 1–10 KHz for sonic logging, and 10–100 Hz for reservoir prediction), is difficult due to the different frequency bands. Once their trends are well quantified, nevertheless, the frequency-dependent characteristics of dispersion and their related attenuation are to be considered as a powerful diagnostic attribute to aid existing inversion approaches in reservoir characterization of the microstructure and pore pressure, as well as seismic monitoring of variations in inhomogeneous fluid saturation distributions and injected CO₂ volume in porous rocks (e.g., Batzle et al., 2006; David et al., 2013; Pimienta et al., 2015, 2016; Li et al., 2019). Various theoretical or modelling solutions have been proposed to understand the frequency effects of wave propagation in fluid-saturated reservoir rocks and their underlying mechanisms (e.g., White, 1975; Gurevich et al., 2010; He et al., 2021; Chen et al., 2022). To the authors' knowledge, however, the experimental verification of the frequency dependence of these models is limited by the lack of experimental data at low frequencies under controlled and comparable conditions.

Most experimental measurements in the laboratory have been traditionally carried out at static (zero-frequency) and ultrasonic (high-frequency) conditions to characterize the dispersive properties of porous rocks. At high frequencies, the stiffest elastic behavior is expected as pore pressures usually have no time to equilibrate, corresponding to the passing of an ultrasonic wave in the laboratory. Owing to the experimental complexities, it has been difficult to obtain laboratory data between these two frequencies under well-designed and controllable experimental conditions with well characterized samples. Over the last few decades, nevertheless, several experimental techniques, including the resonant bar method (e.g., Winkler and Nur, 1979; Gordon and Davis, 2012), the differential acoustical resonance spectroscopy method (e.g., Harris et al., 2005; Wang et al., 2012; Zhao et al., 2015) and the stress-strain method (e.g., O'Connell and Budiansky, 1978; Batzle et al., 2006; Tisato and Madonna, 2012; Madonna and Tisato, 2013; Mikhaltsevitch et al., 2014; Subramaniyan et al., 2014), were proposed to measure the seismic attenuation and the corresponding complex elastic modulus dispersion in additional frequency ranges using specific devices. In particular, the stress-strain measurement technique based on the axial forced oscillation method shows great prospects that allows for directly characterizing the dispersive properties of rocks over broad frequency and pressure ranges and, has recently been the subject of much experimental efforts (e.g., Pimienta et al., 2016; Spencer and Shine, 2016; Szcwcyk et al., 2016; Yin et al., 2017; Sun et al., 2018; Borgomano et al., 2020; Lozovyi and Bauer, 2019). Rock samples, installed in a triaxial setup, are subjected to forced oscillations generated by piezoelectric actuators (PZTs) or dynamic shakers (e.g., Adam et al., 2009; Yin et al., 2017; Sun et al., 2020). And thus, the determination of frequency-dependent attenuation and elastic moduli can be achieved using the phase angle and the ratio, respectively, between the directly measured stress and strain. The stress-strain forced oscillation method, which consists of the vibrating system and sensitive strain transducers, allows for measurements at small-magnitude axial strain oscillations ($<10^{-6}$) measured locally on the samples by the bonded strain gauges, to leave out the non-linear influences associated with crack closure and reopening. Using axial oscillation technique, Spencer (1981) made the first attempt to obtain Young's modulus and attenuation measurements in the frequency range of interest (4–400 Hz) on vacuum dry and fluid-saturated rock samples. A similar experimental apparatus based on the torsional forced oscillations was developed by

Jackson and Paterson (1987) under pressure (25–300 MPa) to measure dispersion and attenuation of shear modulus on calcite within low seismic frequencies, and later modified to conduct the torsional and flexural oscillations (Jackson et al., 2011). Batzle et al. (2006) presented a set of elastic moduli measurements on a dry and glycerin-saturated sandstone over a large frequency and effective pressure range up to about $f \in [5-2500]$ Hz and $P_c \in [7-17]$ MPa, respectively. Their results show that the low-frequency saturated velocities are substantially lower than the high-frequency measurements at ultrasonic frequencies, whereas no frequency dependence of elastic waves and very small pressure dependence are observed under dry conditions as expected. Through a series of laboratory experiments over the range of 1–200 Hz, Spencer and Shine (2016) presented a comprehensive investigation on the effects of permeability and fluid viscosity on modulus dispersion and the associated attenuation in sandstones. The previous laboratory device at the China University of Petroleum (Beijing) can operate at strain amplitude of $<10^{-6}$ and was able to obtain Young's modulus and Poisson's ratio over the 2–200 Hz band.

The improved laboratory device reported herein allows for combined measurements of ultrasonic velocities and the complex elastic moduli of cylindrical samples over a wide range in frequency ($f \in [1-2000, 10^6]$ Hz) and pressure ($P_c \in [0-40]$ MPa) via the stress-strain forced oscillation method, under temperatures between -35 °C and 120 °C. Several stress-strain experiments performed on fluid-saturated sandstones or carbonates have been reported recently (e.g., Yin et al., 2017; Zhao et al., 2019; Long et al., 2020; Sun et al., 2020; He et al., 2022). The main objective of the paper is to present the experimental device itself and report the related measurements on frequency-dependent Young's modulus, Poisson's ratio and their corresponding attenuation. The experimental device and experimental procedure are first described. Then, several experiments are carried out to obtain the frequency- and pressure-dependent measurements on three standard samples for calibrations, a shale sample, as well as on the tight sandstone sample successively saturated with nitrogen, glycerin and brine. The laboratory results mostly speak for themselves and are interpreted in the light of poroelastic and fluid-flow theories.

2. Low-frequency experimental methods

2.1. Seismic elastic moduli module (SEMM)

2.1.1. The broad frequency band elastic moduli setup

In this section, the design of an improved Seismic Elastic Moduli Module located at China University of Petroleum (Beijing), aiming at measuring simultaneously high-frequency (HF) ultrasonic P- and S-wave velocities along the sample axis and low-frequency (LF) dynamic elastic properties (Young's modulus E and Poisson's ratio ν) at low frequencies, is described. The broad frequency band elastic moduli laboratory apparatus SEMM, which is conceptually comparable with the device developed at Colorado School of Mines (Batzle et al., 2006), is theoretically based on the forced oscillation approach. High-frequency properties are measured utilizing the pulse transmission method, while elastic moduli at low frequencies are determined with the use of the stress and strain technique of small axial deformations of $<10^{-6}$ locally measured with resistive strain gauges bonded directly on the sample. A schematic illustration of the mechanical assembly and the photograph of the experimental apparatus SEMM are shown in Fig. 1. SEMM can operate at frequencies of 1–2000 Hz, appropriate for investigating modulus attenuation and the associated dispersion behaviors due to wave propagation in fluid-saturated rocks.

The new apparatus that may be divided into three main units: (i) the multi-frequency band module, (ii) the pressure manifold and

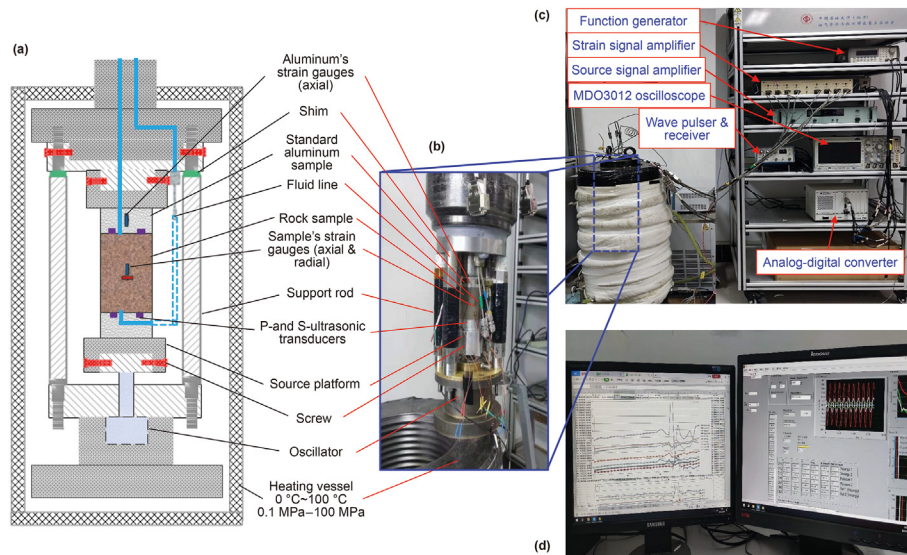


Fig. 1. Schematic representation (a) and photograph (b) of the typical experimental apparatus SEMM. The forced oscillation setups for frequency-dependent elastic dispersion and attenuation measurements (c) are composed of three main components: (i) the multi-frequency band setup, (ii) the pressure manifold and, (iii) the temperature control system. A vessel was designed for loading pressure and temperature. The mechanical unit (b) can be put into the vessel for mimicking *in situ* high-pressure, high-temperature measurements. An actuator is applied as the stress load to generate displacement modulations at seismic frequencies. Two endcaps with built-in compressional and shear wave ultrasonic transducers with central frequency of 1 MHz are settled on the top and bottom surfaces of the sample. (d) Photograph of the computer system for laboratory data acquisition and processing.

(iii) the temperature control system, are strengthened in its measurement repeatability, stability and accuracy with few modifications, compared with a previous module by [Batzle et al. \(2006\)](#). The ambition was to design a laboratory technique for comprehensive determination of frequency dependence of the dynamic Young's modulus E and Poisson's ratio ν for core plugs under isotropic conditions at different confining pressures. In our design, we employ the electromagnetic actuator as the force loading a low-level oscillating sinusoidal axial stress to the jacketed sample, avoiding the bonding together with the core plug using the glue in the initial apparatus. [Fig. 1c](#) illustrates the mechanical units of the low-frequency apparatus, in which our utilized oscillator (Brüel & Kjær, type 4810) with an enhanced load capacity transfers a sinusoidal signal, provided from a computer-controlled function generator (Agilent, type 33210A) and amplified by a source signal amplifier (Brüel & Kjær, type 2718), into the mechanical stress that generates strains in the column assemblage stacked by the test sample, two pairs of PZTs and two endcaps of standard aluminum. In [Fig. 2a](#), the column assemblage is equipped with six pairs of semiconductor strain gauges (BCM, SB-1000-5-P-2) of high gauge factor to provide more reliable strain signals. Two pairs of large strain gauges (i.e., 5 mm length) are bonded on the sample in axial direction and the other two in the radial direction acting as Poisson gauges. The non-dispersive aluminum standard, the strain of which is in phase with the acted stress, is equipped with two gauges in the direction of axial deformation for the phase shift measurements between the radial and axial strain-gauge signals of the sample and the aluminum standard. Identical strain gauges, which are mounted to a one-fourth Wheatstone bridge, are utilized here to eliminate possible bias due to varied gauges. An analog-digital converter (NI, PXI-1033) is utilized to convert the continuous analog-signals, which are outputted from a strain signals amplifier for the weak signals obtained with an electric circuitry (Wheatstone bridge) connecting gauges on the opposite sides of the column assemblage, into digital-signals that are processed and acquired with a signal processing system ([Fig. 1d](#)). A classical processing algorithm, fast Fourier transform, is employed to compute the amplitude and phase of the measured signals at each single frequency.

To carry out stable experiments with effective utilization of pore and confining pressures, the test sample is sealed from the nitrogen gas confining pressure via an impermeable fluorinated ethylene propylene film (FEFP) covered by a thin layer of epoxy, rather than a single thick layer of epoxy used initially. The sticky epoxy may spread gently and uniformly across the surface of the gauges bonded sample, which is coated with a piece of heat shrink plastic tube that can shrink and expel any air bubbles from the epoxy during heating in an oven. Owing to the excellent airtight and nonadherent features of FEFP over which strain gauges are glued, our developed sample sealing technique using two outer coatings contributes to a good isolation of the test sample from nitrogen as a confining gas and a great relief of contact friction between the epoxy and the strain gauges.

Anomalous laboratory measurements due to the non-axial perturbations induced resonances are one of the major concerns when designing the axial stress oscillation apparatus. According to previous analysis (see [Sun et al., 2018](#)), a solution is introduced to mitigate the resonance impact in the new apparatus, via replacing the material of supporting rods to alloy steel and regulating their length of approximately 235.2 mm with several pieces of shims made of the same material for the test sample of length round 72 mm ([Fig. 1](#)). The enhanced laboratory module leads to a robust and stable measurement of stress and strain of rock samples over a broader frequency band through shifting the first resonance frequency beyond the range $f \in [1-2000]$ Hz, which is crucial for a more quantitative investigation of frequency dependence of dynamic elasticities related to pore fluid effects.

Meanwhile, active ultrasonic velocity surveys were conducted using the typical pulse transmission approach at high frequency. Two pairs of in-house built compressional (P) and shear (S) wave piezoelectric ultrasonic transducers with the central resonant frequency of ~ 1 MHz (rise time of 1 μ s) of ~ 8 mm diameter and ~ 2 mm height mounted inside the top and bottom aluminum endcaps (see [Fig. 2a](#)), allow recording the total send-receive travel time ΔT and the received waveforms of an ultrasonic wave along the sample vertical axis. At a considered pressure, the ultrasonic measurements for P- and S-wave velocities of testing cores are performed in

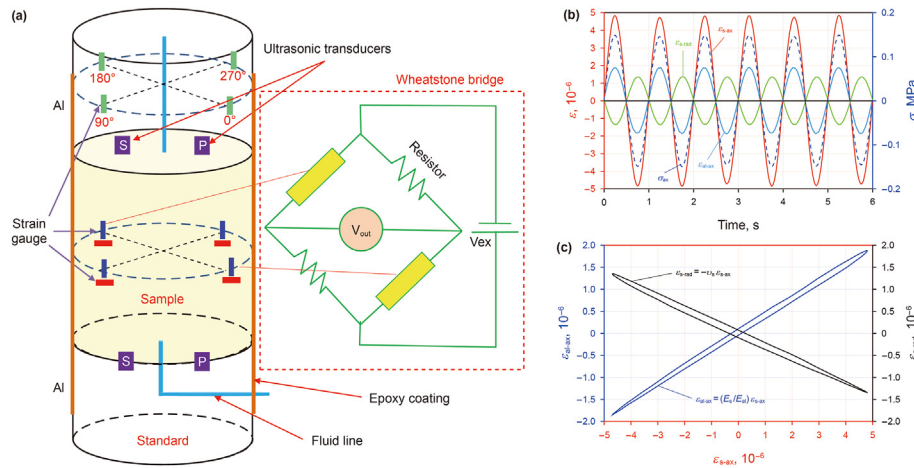


Fig. 2. Schematics of the column assemblage, the key component of the low-frequency system, consisting of the test sample, two pairs of piezoelectric transducers, two aluminum endcaps and a Wheatstone bridge for the weak strain signal output (a) and, typical recordings of axial stress (σ_{ax}) and the standard Aluminum's axial strain (ϵ_{al-ax}) as well as the test sample's axial and radial strains (ϵ_{s-ax} and ϵ_{s-rad}) varying with acquisition time for the dynamic axial-stress oscillations for the lucite sample for a confining pressure of 2 MPa (b) and (c). The linear regressions between the recorded stress and strain curves (c) are employed to calculate frequency-dependent elastic moduli (e.g., Young's modulus E_{1F} and Poisson's ratio ν_{1F}) of the test sample, given the reference aluminum endcaps with the Young's modulus E_{al} of 70 GPa. The test sample, which is attached with semiconductor strain gauges for determining strain in axial and radial direction, is a cylinder of length $L = 65\text{--}85$ mm and diameter $d = 38.1$ mm. The aluminum standard is equipped with two pairs of axial strain gauges for phase shift measurements. Note that the epoxy coating around the sample seals the sample from the nitrogen gas in the cell used for applying confining pressure.

sequence, and followed by forced-oscillation measurements in axial direction under undrained conditions to measure elastic dispersion and attenuation in seismic frequencies.

The vessel equipped with both electronic feedthroughs and fluid lines allows for independent confining and pore pressure control. To study the dynamic elastic properties at varying effective pressures and at elevated temperatures, experimental measurements may be performed via placing the entire mechanical units of Fig. 1b inside a nitrogen gas confining vessel that is used for exerting the confining pressure up to 70 MPa on the column assemblage, through a servo-controlled confining pump linked to the vessel chamber. The confining pressure feedback is obtained with a pressure sensor (Omega, PX602-20KGV) located at the top of the vessel to ensure that the pressure measurement is completely equivalent to that acted to the testing sample. Using a servo-regulated heating bath circulation thermostat placed around the confinement vessel, the laboratory system can adjust vessel temperatures between -30 °C and 120 °C, which is directly measured with a thermal transducer (Omega, SA1XL-K-SRTC) that is placed inside the heating vessel.

2.1.2. Pore pressure setup

For low-porosity and low-permeability shale and tight sandstones, the successful pore pressure regulation may be ascertained with the presented sample sealing technique that provides the sample side drainage condition. Both pore fluid pipes linked to the two aluminum endcaps, small-volume pore pressure sensor with $P_p \sim 0.001$ MPa accuracy and pneumatic valves together constitute the pore pressure unit in the SEMM that is manipulated externally and independently of the confining pressure, by a connected servo syringe pump (Teledyne ISCO, Model 100DM) of pressure and fluid volume measurement accuracy of about $P_p \sim 0.001$ MPa and 0.001 mL, respectively. Since macroscopic fluid flows through rock sample's boundaries can result in great errors for low-frequency experimental measurements, it is therefore crucial to reduce the possible pipeline's fluid volume outside the sample (dead volume), as addressed in Pimienta et al. (2015) and Szweczyk et al. (2016). In the improved laboratory device, we utilize small-sized pore pipes with inside diameter of 0.5 mm, and the pore pressure sensor and valves are placed as close as possible to the test sample. In such a

manner, the measured total dead volumes are minimized to about 3.6 mL, a value sufficiently small for most experimental measurements. In addition, the valves can be closed during the dynamic axial oscillating experiments, such as to carry out undrained experiments as the fluid volumes (sample pore + dead volume) remain constant in the system. This configuration has been proved to be appropriate for most applications (e.g., Batzle et al., 2006; Subramaniyan et al., 2015; Pimienta et al., 2016; Yin et al., 2017; Sun et al., 2020), as any possible uncertainties related to an extrinsically caused differed fluid flow can be eliminated. It is also important to note that because of the existence of fluids within the sample's pores and the pipes, the test sample may remain drained under low frequencies (~ 1 Hz) axial stress oscillation conditions.

2.2. Experimental procedures

2.2.1. Sample preparation

At China University of Petroleum (Beijing), core plugs with a diameter of about 38.1 mm and a length of 65–85 mm were drilled using water as a drilling fluid and trimmed with a surface grinder. This tends to wear grains of weak cementation from the core and, thus, the surface roughness is about ~ 30 μm while the two ends of the sample are flat and parallel to ~ 10 μm . Offcuts from these cores were employed for sample characterization in terms of mineralogy, microstructural evaluation, grain density, grain size distribution and porosity.

In this presented work, three standard samples, a synthetic lucite sample and both pure aluminum and Titanium samples, were chosen to examine the reliability of the SEMM and procedure. It can be generally assumed that these samples, which have been broadly studied in frequency-dependency parameter measurements, are essentially homogeneous and isotropic materials at the sample scale without porosity, indicating that their elastic moduli are not expected to vary with confining pressure or additional axial pressure. In particular, the elastic properties of aluminum and titanium, being much stiffer than aluminum, are believed to be independent of frequency which makes them good test media for dynamic stiffness measurements, whereas lucite made of viscoelastic materials possesses significant frequency dependency and usually is employed as a mean to examine the performance of an attenuation

device (e.g., see Batzle et al., 2006; Pimienta et al., 2016; Yin et al., 2017; Sun et al., 2018). For our sample, the viscous lucite is made of acrylicplastic or polymethylmethacrylate, which has a lower elastic modulus than sandstones. The material has a negligible porosity and the bulk density of about 1195 kg/m³, and its Young's modulus increases by about 38% as frequency increases from 1 Hz to 2000 Hz.

In addition, two porous and elastic core samples, an overburden shale and a tight sandstone, were utilized to study how pressure and pore fluid affect the dynamic elastic properties of tight rocks using the new experimental device. The used dry shale (L shale), which has a porosity less than 3.1%, was extracted from a drill core (3502–3513 m deep) of a caprock formation overlying gas-bearing sandstones. Quantitative mineralogy analysis taken from the X-ray powder diffraction (XDR) tests of the oven-dry shale core shows the studied L shale core consists of about 45% clay, 25% quartz and around 8% carbonates. To assess the frequency-dependent elastic properties of the anisotropic shale core, experiments were performed with three differently oriented cylindrical core plugs drilled from a single batch of overburden materials: the angle between the sample axis and the symmetry axis of the shale (perpendicular to the sedimentary bedding) was 0°, 45° and 90°. Once cored and followed by drying in an oven for 24 h at 76 °C, the specimens were exposed to an environment with controlled relative humidity (RH) for 48 h and then placed inside the desiccators to maintain the pore fluid saturation. Laboratory experiments were prepared and conducted in their native state (corresponding to approximately 66% saturation) after the core plugs were stabilized at room temperature of ~20 °C and the mass variations did not vary more than 0.01 g over the course of 1 week for about 4 weeks.

Furthermore, the tight sandstone specimen used in this study was sampled from an onshore well drilled from a hydrocarbon reservoir in Eastern China at a depth of 3221–2230 m. XDR data shows that the tight sandstone sample, with mineral compositions and physical properties listed in Table 1, is mainly made of around 76.8% quartz, 7.6% feldspar and 5.16% calcite. Via the Voigt-Reuss-Hill average, elastic moduli of solid grains were determined using the volumetric contribution of each mineral and their respective elastic properties. The interconnected porosity, $\varphi = 8.83\%$, and permeability, $\kappa = 0.032$ mD, of the dry sample were quantified with helium as the reference fluid. Note that the non-measurable porosity must be constituted by exceedingly thin pore throats that helium is not capable of penetrating through them. The rock's fluid transport property is an important factor controlling the fluid-flow effects at sample scale. The experimental determination of tight core sample's permeability was accomplished using the fluid pressure gradient approach, which consists of measuring the fluid flow after applying a pressure gradient. Rock permeability can be

Table 1

Rock material parameters of the tight sandstone sample used in this experimental study. Porosity and permeability were measured at 2 MPa effective pressure and at 23.1 ± 0.2 °C.

Porosity, %	8.83	Clays, %	5.42
Density, kg/m ³	2360	Calcite, %	5.16
Helium permeability, mD	0.032	Muscovite, %	2.31
Length, mm	75.2	Dolomite, %	4.1
Diameter, mm	38.1	Bulk modulus of solid grains, GPa	42.6
Quartz, %	72.8	Shear modulus of solid grains, GPa	30.26
Feldspar, %	7.6	Solid grain density, g/cm ³	2.763

sample mounting time within less than 30 min after exposing the core plugs to air from the desiccators. In our designed device, strain gauges are bonded onto the sample surfaces with sticky epoxy to keep the gauges fixed during the sample sealing and, in particular, to achieve a better coupling between the sample and gauge during dynamic oscillation experiments over several months under influences of different saturation fluid, pressure and temperature, although the actual mechanical coupling is primarily exerted by the confining pressure. In addition, for the ease of sample gluing and sealing with the prepared epoxy resin, a mould made of plexiglass was developed to ensure that the 12 electric wires connected to the 6 pairs of strain gauges bonded on the sample are able to be fed out. Plenty of measurements prove that this sample sealing technique provides the seals with great airtightness.

2.2.2. Dispersion and attenuation measurements

In the SEMM, combined with the length of the testing sample L , the high-frequency compressional and shear-wave velocities (i.e., V_{P-HF} and V_{S-HF}) in the axial direction of the core are determined from the laboratory standard measurements (~1 MHz) by

$$V_{P,S} = \frac{L - \Delta L}{T - T_0}, \quad (1)$$

where ΔL represents the sample length change due to the applied axial force and T_0 represents the correction for the system travel time. The average times of a repetition of four times are used as the final measured values. The relative errors between successive compressional and shear velocity measurements using the SEMM are roughly less than 1% and 2%, respectively. The corresponding bulk modulus K_{HF} , shear modulus μ_{HF} , Young's modulus E_{HF} and Poisson's ratio ν_{HF} can be inferred from the measured ultrasonic velocities throughout the following equations

$$K_{HF} = \rho V_{P-HF}^2 - 4/3 \rho V_{S-HF}^2 \text{ and } \mu_{HF} = \rho V_{S-HF}^2,$$

$$E_{HF} = 9K_{HF}\mu_{HF} / (3K_{HF} + \mu_{HF}) \text{ and } \nu_{HF} = (3K_{HF} - 2\mu_{HF}) / (2(3K_{HF} + \mu_{HF})), \quad (2)$$

directly calculated based on Darcy's law (e.g., see Pimienta et al., 2015), with the sample's dimensions and the gas viscosity being input parameters.

For the laboratory investigation of the influence of fluid on frequency-dependent elastic characteristics in tight core samples, it is crucial that the pore fluid saturation state of the specimens is preserved appropriately, which thus requires fast sample mounting. The designed clamp holder for ease of sample and strain gauges bonding operation (see Yin et al., 2017), together with the proposed sample sealing technique, allows minimizing the test

here bulk density of the saturated rock $\rho = \rho_f \times \varphi + \rho_m \times (1 - \varphi)$ is defined with the known densities of the dry matrix (ρ_m) and saturating fluid (ρ_f), and the rock porosity (φ).

As described above, the low-frequency measurements depending on the stress-strain method can directly yield the dynamic elastic moduli K_{LF} , μ_{LF} , E_{LF} and ν_{LF} . When a sinusoidal stress at a specific frequency is exerted to the test sample, strain modulations at both radial and axial directions can be measured by the bonded gauges and acquired by the computer. In the SEMM, four

pairs of strain gauges are mounted in a one-fourth Wheatstone bridge, allow averaging the strains on the opposite side of the sample. Typical recorded measurements of axial stress (σ_{ax}) as well as strains in axial (ε_{al-ax} and ε_{s-ax}) and radial (ε_{s-rad}) directions during continuous axial-stress oscillations are displayed in Fig. 2b and 2c. The axial stress value (σ_{ax}), which is equally loaded along the assemblage (the sample + the aluminum endplate) and is controlled by the exerted force magnitude (F) and the cross-sectional area of core sample (S), can be calculated by

$$\sigma_{ax} = \sigma_s = \sigma_{al} = F/S. \quad (3)$$

In addition, during the low-frequency measurements, changes in length of the strain gauges, due to continuous forced-oscillations induced strains, lead to resistance variation in this way that strains ε on the standard aluminum and on the rock sample result in changes of output voltage V_{out} through the Wheatstone bridges with the half-bridge configuration, and can be extracted by

$$\varepsilon = 2 * V_{out} / (V_{ex} * SC * AM), \quad (4)$$

where V_{out} denotes output, V_{ex} denotes the supply voltage for the bridges, SC denotes the sensitivity coefficient of strain gauges, and AM denotes the magnification of signal amplifier. From our experience, the recorded strains ε in the low-frequency measurements are normally round 10^{-8} – 10^{-7} , less than 10^{-6} .

$$Q_S^{-1}(\omega) = Q_E^{-1}(\omega) + \nu(\omega)/(1 + \nu(\omega)) * Q_v^{-1}(\omega)$$

$$Q_P^{-1}(\omega) = (1 + \nu(\omega))/((1 - \nu(\omega)) * (1 - 2\nu(\omega))) * Q_E^{-1}(\omega) - 2\nu(\omega) * (2 - \nu(\omega)) * Q_S^{-1}(\omega) / (1 - 2\nu(\omega)) \quad (9)$$

$$Q_K^{-1}(\omega) = (3 * Q_E^{-1}(\omega) - 2 * (1 + \nu(\omega)) * Q_S^{-1}(\omega)) / (1 - 2\nu(\omega))$$

With both axial and radial strain amplitudes, $\varepsilon_{s-ax}(\omega)$ and $\varepsilon_{s-rad}(\omega)$, sensed dynamically by the strain gauges bonded on the samples' surface (Fig. 2b), the low-frequency Young's modulus $E_{LF}(\omega)$ of the stressed sample is extracted using the Young's modulus of the aluminum standard E_{al} and the ratio between the aluminum and rock strains (Batzle et al., 2006),

$$E_{LF}(\omega) = \sigma_s / \varepsilon_{s-ax} = \sigma_{al} / \varepsilon_{al-ax} = E_{al} * \varepsilon_{al-ax}(\omega) / \varepsilon_{s-ax}(\omega), \quad (5)$$

where the complex modulus E_{al} relates the stress σ_{al} to its resulting strain ε_{al} via $\sigma_{al} = E_{al} * \varepsilon_{al}$, which can be estimated from the known Young's modulus of the aluminum standard E_{al} with its measured strain ε_{al} . Furthermore, Poisson's ratio $\nu_{LF}(\omega)$ of the stressed sample can be estimated using the strain amplitudes of the sample,

$$\nu_{LF}(\omega) = - \frac{\varepsilon_{rad}(\omega)}{\varepsilon_{ax}(\omega)}. \quad (6)$$

In addition, wave attenuation is often characterized using the inverse quality factor Q^{-1} , which can be used to measure the dissipated elastic energy during low-frequency stress oscillation measurements. Considering the pure elasticity of the aluminum endplate, its strain is exactly in phase with the exerted force. The phase of the applied stress can be represented with the phase of strain of the aluminum endplate. And thus, for the complex Young's modulus E , the corresponding extensional attenuation $1/Q_E$ can be calculated using the relation

$$Q_E^{-1} = \text{Im}(E) / \text{Re}(E) = \text{Im}(\sigma_{al} / \varepsilon_{s-ax}) / \text{Re}(\sigma_{al} / \varepsilon_{s-ax}) = \tan(\theta_{\varepsilon_{al-ax}} - \theta_{\varepsilon_{s-ax}}), \quad (7)$$

here $\theta_{\varepsilon_{al-ax}} - \theta_{\varepsilon_{s-ax}}$ represents the phase shift between the axial strains of the standard aluminum and the sample. Analogically, Poisson's ratio associated attenuation $1/Q_\nu$ can also be inferred $1/Q_\nu = \tan(\theta_{\varepsilon_{s-rad}} - \theta_{\varepsilon_{s-ax}})$, where $\theta_{\varepsilon_{s-ax}} - \theta_{\varepsilon_{s-rad}}$ denotes the phase shift between the axial and radial strains on the sample. Note that $1/Q_\nu$ may not considered as an attenuation factor, as the elastic Poisson's ratio ν is not a stiffness.

Via assuming the material is homogeneous and isotropic, we can calculate P-wave, bulk and shear moduli (i.e., $P_{LF}(\omega)$, $K_{LF}(\omega)$ and $\mu_{LF}(\omega)$), the two independent elastic parameters, from the measured complex Young's modulus and Poisson's ratio using the well-known relations

$$K_{LF}(\omega) = E(\omega) / [3 * (1 - 2\nu(\omega))]$$

$$\mu_{LF}(\omega) = E(\omega) / [2 * (1 + \nu(\omega))]$$

$$P_{LF}(\omega) = K(\omega) + 4\mu(\omega)/3. \quad (8)$$

The associated bulk, compressional and shear wave attenuation can be estimated using the following relations (e.g., see Adam et al., 2009; Spencer and Shine, 2016)

here Q_P , Q_S , and Q_K are the P-wave, S-wave and bulk quality factors, respectively. Furthermore, it is easy to infer the compressional and shear wave velocities, $V_P(\omega)$ and $V_S(\omega)$, from Eq. (8) with the obtained bulk density ρ as follows

$$V_P(\omega) = (P(\omega)/\rho)^{1/2} \text{ and } V_S(\omega) = (\mu(\omega)/\rho)^{1/2}. \quad (10)$$

Through the integration of the ultrasonic pulse transmission technique and the forced-oscillation based stress-strain approach, on the whole, the SEMM at China University of Petroleum (Beijing) has the capability of carrying out modulus dispersion and attenuation experiments of saturated core samples with different fluids over a wide range of frequency and confining pressure.

2.2.3. Possible sources and magnitudes of experimental errors

Throughout this presented work, there is no editing of the measured results at ultrasonic and low-frequency. The estimated errors in the ultrasonic P- and S-wave velocities may stem related to: (i) the uncertainties in the true length of the test sample due to the acted axial stress, (ii) the misalignment of the ultrasonic transducers with respect to the bedding orientation, (iii) the uncertainties in manual first arrival time pick-up of the compressional and shear waves during successive velocity surveys. Deviations in the measurements of V_{P-HF} and V_{S-HF} are propagated to the estimations of high-frequency elastic moduli K_{HF} and μ_{HF} . It is challenging to evaluate the typical values of the accuracy for the measured elastic properties, as the SEMM performance relies on

the chosen core sample itself and sample preparation, as well as factors related to noise magnitude of the electronic signals and strain sensor responses. Although possible bias associated with advice electronic noises may be successfully discarded via using the half-bridge strain-gauge interchanged circuits (Wheatstone bridges), strain gauges themselves can introduce gross errors of 5% considering that their gauge factor and resistivity are very sensitive to pressure and temperature. The perturbations in strain gauge responses lead to deviated output voltage and hence, affecting the Young's modulus and Poisson's ratio measurements. In addition, as all crustal rocks are inhomogeneous and/or anisotropic to a certain extent at the representative elementary volume (REV), sample heterogeneity is potentially the most obvious source of deviations in the axial forced-oscillation experiments. The obtained low-frequency elastic properties via using such local strain measurements by the gauges directly bonded on the sample, which have a maximum resolution of 0.5×10^{-7} , are often inconsistent with those measured moduli at ultrasonic frequency from the bulk average of an entire sample's properties. Under favorable circumstances, the large dispersion of dynamic rock moduli between ultrasonic and low-frequency results in our measurements are largely attributed to the sample heterogeneity effect on a size larger than the scale of the strain gauge, especially for dry cores. Meanwhile, the presence of a fluid dead volume at samples' endplates, as well as the associated fluid over-pressure that cannot be relaxed completely, can possibly cause measuring errors at low frequencies. During our forced-oscillation measurements, the sample intrinsic fluid storage and the minimum dead volume that holds 6.8% of the total pore volume of the sand sample are both kept constant via closing the servo pumps and the valves outside the manifold.

Possible misalignment of the device with the axial stress, which is often associated with the sample surface roughness caused tilt of the sample, is another important source of error in experimental measurements via generating nonuniform distribution of stress and strain states in the column assemblage. Polishing the top and bottom surfaces of the plug sample is necessary to ensure that its two flat ends are rectified to be perfectly parallel in this way the misalignment error can be minimized. In our experiments, the non-parallelism deviation for the core sample preparation is ≤ 0.001 mm, within the tolerable measurement errors. In addition, sample preparation issues (bad strain gauges bonding, damaged epoxy coatings, etc.) and the possible system resonances (see Sun et al., 2018) may cause strong disrupting responses. Tests on non-porous materials of the aluminum sample with its known elastic properties, for quantifying all possible errors, indicate that the experimental errors for Young's modulus and Poisson's ratio are within about $\pm 3.1\%$.

2.2.4. Measurement protocol

Once the sample preparations (i.e., bonding strain gauges on the sample surface, coating the sample with epoxy, mounting between the endplates, and linking gauges with Wheatstone bridges) have been done, the column assemblage in Fig. 2a is placed inside the confinement vessel, so that both confining and pore pressures can be exerted to the test sample with independent controls. The confining pressure can be set as high as 30 MPa, based on the

maximum pressure bearing capacity of the dynamic shaker. The pore pressure that is manipulated by a servo syringe pump linked to the sample via pipelines is maintained constant at $P_p = 1.5$ MPa. The effective pressure that is defined here as $P_{\text{eff}} = P_c - P_p$, is changed generally by changing the confining pressure at a regulated rate of round 0.41 MPa/min. To avoid the occurrence of instantaneously high pore pressure region during pressurization process, pressures exerted by compressed nitrogen gas are maintained constant over ~60 min that allows for complete equilibration of the pore pressure. A series of experiments have been carried out in which fluid effect on the elastic moduli over a wide pressure and frequency range are investigated, using natural cored porous rocks including shale cores and a tight sandstone sample that was measured sequentially under dry (nitrogen gas), brine and glycerin saturated conditions. The physical properties of the pore fluids are summarized in Table 2. In addition, in order to achieve stable measurements at low frequencies, it is necessary to calibrate the laboratory device using elastically homogeneous and isotropic samples with known elastic moduli prior to carrying out forced-oscillation measurements on porous core plugs. Under normal conditions, according to previous applications on tight sandstones (e.g., Yin et al., 2017; Zhao et al., 2019; Sun et al., 2020), the mean errors in the modulus dispersion and attenuation (inverse quality factor) are roughly $\leq 3.5\%$ and within about ± 0.0005 , respectively. Please also note that all the experimental tests were conducted at the air conditioning of the room temperature of 23 °C and at various differential pressures, instead of attempting to imitate the true subsurface conditions, which is impossible given the depth of the drilled core samples.

A procedure similar to the previous applications (e.g., Pimienta et al., 2015; Yin et al., 2017) was proposed to evaluate the pressure and frequency dependence of the dynamic elastic properties of core plugs dry and then saturated with fluid. Starting from an effective pressure of round $P_{\text{eff}} \sim 1$ MPa, two to three times forced-oscillation measurements (Fig. 1) of the elastic moduli on the purely elastic and homogenous aluminum, titanium and lucite samples (primarily for calibration), and porous core plugs of dry (humidified), saturated with liquid glycerin and brine were conducted in sequence at each given effective pressure level step up to the maximum confining pressure. Following these low-frequency measurements, ultrasonic arrival times of compressional and shear waves between the top and bottom surfaces (Fig. 2) were measured to extract the corresponding high-frequency velocities and elastic moduli.

Experimental measurements on humidified sample saturated with nitrogen gas were performed first to examine the frequency effects on the average of elastic moduli of the dry sample. Owing to the truth that even gas reservoirs usual have irreducible water content in the pore volume of no less than ~1%, which may significantly affect the rock elastic moduli and attenuation via weakening the rock frame, we introduce water vapor of around ~1% saturation in pore space to the oven dry sample. Dry core samples were initially humidified via storing them in a humidifying chamber at 99% humidity over a period between 7 and 14 days, to obtain matrix softening due to moisture in the pores. Note the length of the duration relies on the permeability and pore surface area of the sample that determines the rock sensitivity to water vapor (e.g., Adam et al., 2009).

Subsequently, dynamic elastic properties of the glycerin-saturated sandstone were measured in the SEMM at the same temperature and effective pressures as the dry condition, via injecting liquid glycerin into the tight core plug. A vacuum pump connected to the top sample end is utilized to create a vacuum condition inside the sample, at which the feedbacked pressure P_p reaches a stable negative level of round -0.5 MPa. And then,

Table 2

Physical properties of pore fluids used in this experimental study (at 1.2 MPa and 23 °C).

Pore fluid	Bulk modulus, GPa	Viscosity, 10^{-3} Pa s	Density, kg/m^3
Nitrogen (gas)	1.36×10^{-3}	0.0172	11.50
Glycerin	4.586	1410.063	1252.2
Brine	2.28	1.0226	1013

glycerin is injected into the sample through the connected pipe to the bottom sample under vacuum condition via the vacuum pump. In this way the injection procedure relieves the density effect by expelling air with the denser fluid and hence, allowing for a glycerin full saturation. The fluid injection rate is regulated by connected servo syringe pumps to strictly quantify the liquid volume flowed into the sample. When there has no more flow from the fluid pump through the sample, we assume that a full saturation state is achieved.

Finally, brine full saturation is ascertained by directly injecting the brine solution with salinity of 18,000 ppm NaCl in the glycerin-saturated sample plug. Considering liquid glycerin may almost momentarily and completely dissolves in water, thus converting to

nonviscous fluid, the full brine saturation can be accomplished via flushing two to three times the pore volume. The sample was then tested the same procedure as for the glycerin saturation case.

3. Calibration results: measurements under different pressures

3.1. Effects of confining pressure and frequency on the reference samples

The three completely homogeneous and isotropic samples (aluminum, titanium and lucite) described above for calibration were utilized to assess the measuring accuracy of the new

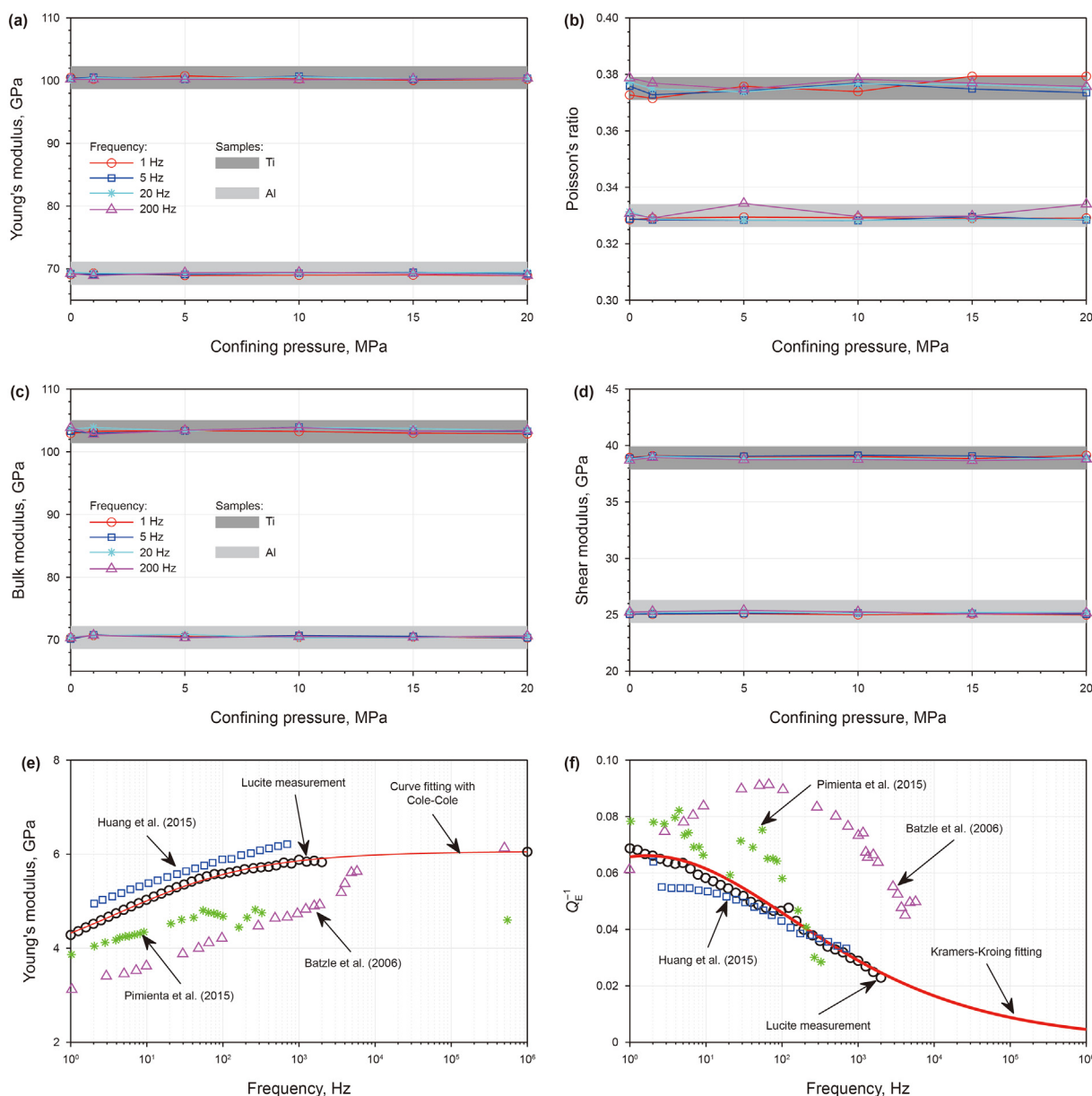


Fig. 3. Measured pressure and frequency dependence of the elastic properties for the three reference samples of titanium, aluminum and lucite from axial-stress oscillations with SEMM. The two standard samples' Young's modulus (a) and Poisson's ratio (b) at four different oscillation frequencies of $f = 1, 5, 20, 200$ Hz are directly measured at all confining pressures up to 20 MPa. The inferred bulk (c) and shear (d) moduli of the two standard samples are compared with the earlier measurements on the nonporous standard samples (e.g., Batzle et al., 2006; Huang et al., 2015; Szweczyk et al., 2016; Yin et al., 2017). The calibration results of Young's modulus (e) and the corresponding extensional attenuation (f) for the lucite sample as a function of frequency at a confining pressure of 2 MPa are illustrated, together with the literature data from Batzle et al. (2006), Huang et al. (2015) and Pimienta et al. (2015) for a comparison. Parametric fits are applied to the experimental data and subsequently employed to calculate Young's modulus E and attenuation $1/Q_E$ based on the Cole-Cole and Kramers-Kroing relations, respectively.

laboratory apparatus SEMM and the proposed procedure. Two pairs of orthogonal biaxial strain gauges were bonded at the length center of the sample. The results of laboratory measurements for the three standard samples as a function of confining pressure for given frequencies are demonstrated in Fig. 3, along with the static values in previous literatures. The measured high-frequency data at 1 MHz are estimated using Eq. (2). Please also note that a small axial stress of about 0.3 MPa was applied during all measurements to avoid the possible stress-induced non-parallelism of the column assembly and ascertain the experimental stability (e.g., Subramanian et al., 2015).

For the nonporous aluminum and titanium samples with known elastic properties, the Young's modulus (Fig. 3a) and Poisson's ratio (Fig. 3b) measurements are independent of the exerting confining pressure, which are in a good agreement with the published results. Moreover, the absence of modulus dispersion is confirmed for both samples at all measuring frequencies within the seismic band. The results are in accordance with the non-dispersive properties of aluminum and titanium, which can be considered as purely elastic materials under the applied pressure and the measured frequency range and thus valuable test media for dynamic elastic measurements.

In addition, the bulk modulus K_{LF} and shear modulus μ_{LF} which can be inferred by combining the measured E_{LF} and ν_{LF} under the assumption of elastic and isotropic materials using Eqs. (5) and (6), are summarized in Fig. 3c and 3d, respectively. For the two standard samples, bulk and shear moduli computed in this study are compared with the previous measurements (e.g., Batzle et al., 2006; Szewczyk et al., 2016; Yin et al., 2017). We observe that K_{LF} and μ_{LF} measurements in the SEMM fit well with values in previous measurements using different laboratory apparatuses, indicating that the stability and repeatability of the measurements using different devices can be achieved.

Furthermore, the frequency dependence of lucite is examined here, via the measured Young's modulus E_{LF} and its associated attenuation $1/Q_E$, to further assess the reliability and reproducibility of our new device. As illustrated in Fig. 3e, we find that Young's modulus of lucite increase from low seismic to high ultrasonic frequencies. The modulus dispersion measurements are mainly related to the viscoelastic dispersive characteristics of lucite. Please note the continuously increasing trend of Young's modulus E_{LF} over the higher frequencies of 200–2000 Hz is observed in the SEMM of sufficiently broad frequency range, compared to the measurements in Yin et al. (2017). Although the frequency dependence of this synthetic lucite may vary from sample to sample considering the materials are not exactly the same, the values presented in literatures on this material (e.g., Batzle et al., 2006; Huang et al., 2015; Pimienta et al., 2015) are displayed for comparisons with our measurements. We find a similar trend between our measurements and the published data, although with observable discrepancies probably due to the difference in the sample media and the different conditions of each laboratory measurements.

In addition, considering that the measurements of Young's modulus and the extensional attenuation occur in the same frequency band and are independent in the SEMM, it is necessary to examine whether the quantitative relation between the measured E_{LF} and $1/Q_E$ are consistent with the causality principle. To the authors' knowledge, the causality principle is often mathematically described via Kramers-Kronig relations (KKR), which link real and imaginary compartments of a complex elastic modulus that controls wave propagation in a medium. We fit the Young's modulus results based on the real part of Cole-Cole relation, as it extrapolates unknown data between the low- and high-frequency limits (Cole and Cole, 1941). And then the imaginary part of the Young's

modulus E''_{LF} is determined from its real part E'_{LF} through the typical Kramers-Kronig relationship (e.g., Mikhaltsevitch et al., 2016b)

$$E''_{LF}(\omega) = \frac{\pi}{2} \frac{dE'_{LF}(\omega)}{d\omega}. \quad (11)$$

Given the real and imaginary parts of Young's modulus E , the extensional attenuation (inverse quality factor) $Q_{E-KK}^{-1}(\omega)$ related to the phase shift $\varphi(\omega)$ between the applied stress and the resulting strain can be determined by (e.g., see Nowick and Bery, 1972; Chapman et al., 2016)

$$Q_{E-KK}^{-1}(\omega) = \frac{E''(\omega)}{E'(\omega)} = \tan(\varphi). \quad (12)$$

The parametric fit of the Young's modulus and the extensional attenuation curves extracted from Eqs. (11) and (12) are displayed in Fig. 3e and 3f. Although the fitting approach considers the frequency dependence of Young's modulus E , we observe that the estimated attenuation curve is good in line with the measured data over the broad frequency range. This demonstrates that the quantitative relation between our laboratory measurements of Young's modulus and extensional attenuation is consistent with the causality principle in terms of the KKR. This implies that our measurements for the lucite sample are causal, and thus the modulus dispersion and attenuation behaviors can reflect the intrinsic nature of the sample considered.

3.2. Sample size and sealing effects for the aluminum sample

Forced-oscillation experimental measurements were further carried out on the aluminum sample, with the aim to check the sample size and sealing effects on the frequency dependency of the Young's modulus and the Poisson's ratio measurements. For the two aluminum samples of the same material with known Young's modulus $E = 70$ GPa, the Young's modulus $E_{LF}(\omega)$ and Poisson's ratio $\nu_{LF}(\omega)$ measurements under a confining pressure of 2 MPa are independent of frequency over a wide range of $f \in [1-1000, 10^6]$ Hz, as shown in Fig. 4a and 4b. In particular, we notice that the measured Young's modulus and Poisson's ratio for the aluminum plug-1 of diameter $D = 38.1$ mm and length $L = 75.6$ mm are slightly larger than the corresponding measurements for the aluminum plug-2 of 25 mm diameter and 51.3 mm length. And the described laboratory device SEMM herein uses relatively large sample plugs of 38.1 mm diameter and length $L \approx 2 \times D$ (about 65–85 mm). In this way, the possible effects of multimillimeter- and centimeter-scale heterogeneities up to the sample length (microstructure of the grain contacts and cracks) on the frequency- and pressure-dependent elastic properties can be measured subtly, according to the studies in Spencer and Shine (2016) and Sun et al. (2020).

Furthermore, we performed a duplicate set of low-frequency experiments to assess the accuracy and repeatability of the SEMM, for two aluminum standards without and with coating the sample with an epoxy via the new sealing technique. It was found that the differences between the Young's modulus and Poisson's ratio measurements on the two aluminum standards without and with coating layers, nevertheless, are negligible. Thus, the new coating can be utilized appropriately in the SEMM, as the influence of the epoxy layer on dynamic elastic moduli is insignificant (having errors of within $\pm 1.6\%$) for the homogeneous and nonporous material (Fig. 4c and 4d). Hence, calibration of the new device with the three nonporous standard samples indicates that the Young's modulus and Poisson's ratio and the associated attenuation can be measured accurately over a large frequency and effective pressure range, up to about $f \in [1-1000, 10^6]$ Hz and $P_c \in [0-20]$ MPa, respectively.

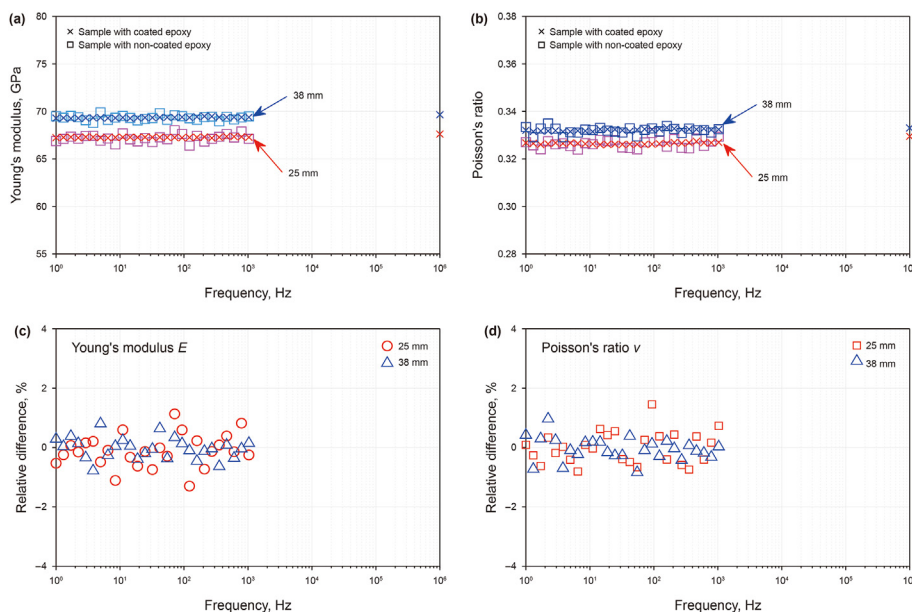


Fig. 4. Frequency-dependent Young's modulus E_{LF} (a) and Poisson's ratio ν_{LF} (b) from the standard aluminum core of diameters $d = 25$ and $d = 38$ mm measured for samples with coated epoxy (crosses) and non-coated epoxy (squares). The experimental measurements were conducted under a confining pressure of 2 MPa in the SEMM. The corresponding relative differences between the measurements obtained with coated and non-coated epoxy for Young's moduli (c) and Poisson's ratios (d) are illustrated.

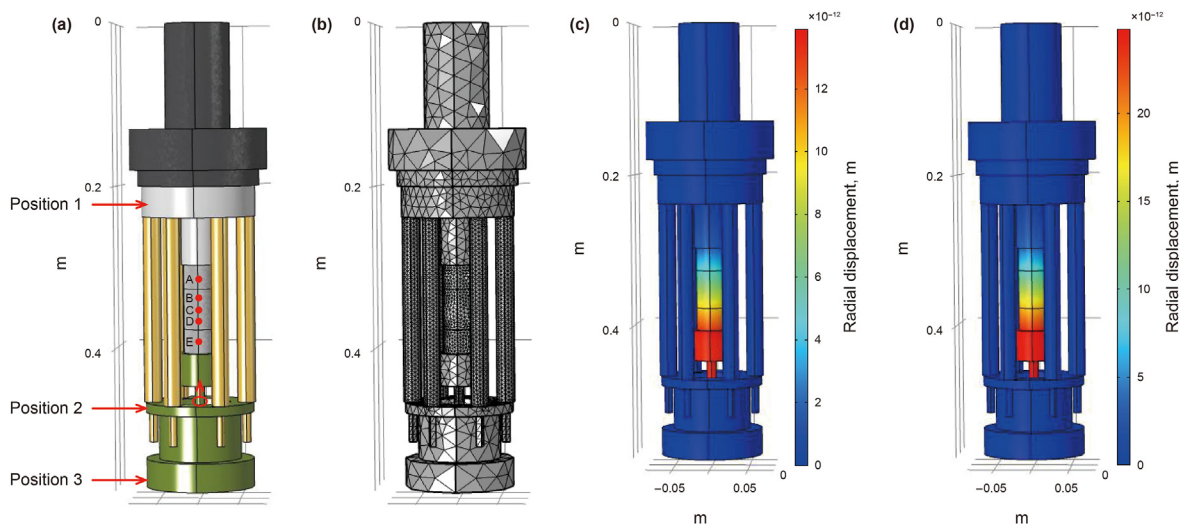


Fig. 5. Numerical model (a) designed to simulate the working process of the experimental apparatus SEMM in Fig. 1, and (b) the corresponding unstructured triangular mesh. The mechanical measurement system, whose materials are purely isotropic and elastic, is solved using finite-element modelling algorithm in the frequency domain for the distribution of the radial displacements. Comparisons of the radial displacements between two non-resonant frequencies of (c) 15 Hz and (d) 300 Hz. In addition, Positions 1, 2 and 3 are three platforms corresponding to the top and bottom of the oscillator housing and the bottom of the vessel head.

3.3. Numerical simulation and frequency dependence analysis

As addressed in Madonna and Tisato (2013), in the context of forced-oscillation experiment the presence of sample heterogeneities in the solid and/or fluid phase may result in a measuring error, considering that the rock volumetric strain and the local strain collected using gauges with dimension of about $1 \times 5 \text{ mm}^2$ bonded on the sample can possess important differences. It is thus reasonable to believe that the local dynamic elastic moduli measurements, which can be precisely extracted with these strain gauges, may often differ from the bulk average. To understand the position (z) dependence of frequency-dependent stress and strain, we conducted numerical simulations on the same aluminum

sample for calibration (diameter $D = 38.1$ mm, length $L = 75.6$ mm, Young's modulus $E = 70$ GPa, and Poisson's ratio $\nu = 0.33$), based on the finite-element commercial software COMSOL Multiphysics. Our modelling of the relevant parts of the experimental module and the sample's dynamic responses follows the philosophy of Sun et al. (2018) and Borgomano et al. (2020). Specifically, we created a numerical model to represent the main mechanical compartment of the SEMM made of alloy steel (Young's modulus $E = 204$ GPa, Poisson's ratio $\nu = 0.28$, and density $\rho = 7.84 \text{ g/cm}^3$) and the column assemblage (Fig. 5a). The fixed boundary condition is mechanically fulfilled, which is possible due to the simulated fixed boundaries at Position 1, Position 2 and Position 3. Meanwhile, boundary conditions of continuous stress and displacements are employed at the

interfaces of the column assemblage, which were bonded hard with epoxy. Additionally, as introduced earlier, an axial preload of 0.3 MPa was exerted to ensure a good contact between each other. In this way, the test sample and the aluminum endplates can freely expand radially, while the lateral displacements are not allowed.

An unstructured mesh composed of tetrahedral elements was employed to discretize the whole numerical model (Fig. 5b). The numerical solution for displacements at each node were obtained in the frequency domain. Analogous to the laboratory experiments, the test sample's radial and axial strains were calculated from the grids' displacements at specific position on the sample's local surface. As well, the axial strains of the aluminum endplates were deduced from the surface node at a specific position on the endplate. The stress and strain state of the vertical column can be represented using the following relations

$$-\rho\omega^2\bar{U} = \nabla \cdot \bar{S} \text{ and } \bar{S} = \bar{C}\bar{\epsilon} = \bar{C}\nabla\bar{U}, \quad (13)$$

here $\omega = 2\pi f$ denotes the angular frequency, \bar{C} denotes the elastic tensor related to the model materials, and \bar{U} and \bar{S} denote the displacement and stress tensors, respectively. In the simulations, the fixed boundary condition at the surface at position 1 is provided by the pressure vessel, and the surfaces indicated as position 2 and position 3 are fixed with two added fixators (Fig. 5a), which can be expressed as

$$\bar{U}_{\text{position1}} = \bar{U}_{\text{position2}} = \bar{U}_{\text{position3}} = 0. \quad (14)$$

In Fig. 5c and 5d, the simulated axial displacement distributions for the measurement system performing at two non-resonant frequencies of 15 Hz and 300 Hz are illustrated. Since the loaded axial stress from the source platform as indicated by the red arrow is assumed to be uniform through the sample and the aluminum endplate along the column's central axis (Fig. 5a), we solely focus on stress and strain state evolutions recorded by strain gauges bonded at the five positions on the vertical column due to axial stress oscillations performed by the shaker, using all possible

known parameters of the laboratory device. And finally, the Young's modulus and Poisson's ratio of the aluminum sample were inferred from the average numerical results based on Eqs. (5) and (6).

The simulated stress and strain amplitude results, deduced from the virtual strain gauges at five reference positions of the column assemblage, are displayed in Fig. 6a and 6b, respectively, over the frequency range of interest $f \in [1-2000]$ Hz. It appears that there are no differences between the exerted stresses from gauges bonded at the 3 different positions on the aluminum sample (i.e., B, C, and D in Fig. 6a) up to 1000 Hz. As well, we observe that the sample's axial strains at the 3 positions are identical, and the corresponding radial strains have the same magnitude. The strain amplitude results between the 2 endplates show slight divergency. These simulation results verify the assumption that the exerted axial stress is uniformly distributed through the test sample, and illustrate that the induced strain magnitudes in axial and radial directions may not be significantly affected by changing the sample's strain gauges position z within the frequency range of interest for the standard aluminum.

The inferred Young's moduli ($E(\omega) = E_{\text{al}} * \epsilon_{\text{al-ax}}(\omega) / \epsilon_{\text{s-ax}}(\omega)$) of the aluminum sample and the Poisson's ratios ($\nu(\omega) = -\epsilon_{\text{rad}}(\omega) / \epsilon_{\text{ax}}(\omega)$) at five positions of the column assemblage are compared with the $E(\omega)$ and $\nu(\omega)$ measured experimentally on the same sample. Via using the same $\epsilon_{\text{al-ax}}$ of the endplate, we find that the simulated Young's moduli results from the three strain gauges at different positions have the identical magnitude. It appears that $E(\omega)$ using the $\epsilon_{\text{al-ax}}$ of position E, which is consistent with the laboratory measurement, is slightly larger than the inferred $E(\omega)$ using $\epsilon_{\text{al-ax}}$ of position A. As no obvious phase shift between the strains on the sample and the aluminum endplate was induced by the homogeneous stress and strain fields in the vertical column at normal frequencies (Fig. 6c and 6d), we observe theoretically expected negligible dispersion characteristic of the sample's Young's modulus.

Furthermore, the simulated Poisson's ratio $\nu(\omega)$ of the aluminum sample, which fits the measured $\nu(\omega)$ and has no divergency for the three positions, is slightly larger compared to $\nu(\omega)$ at Position E of

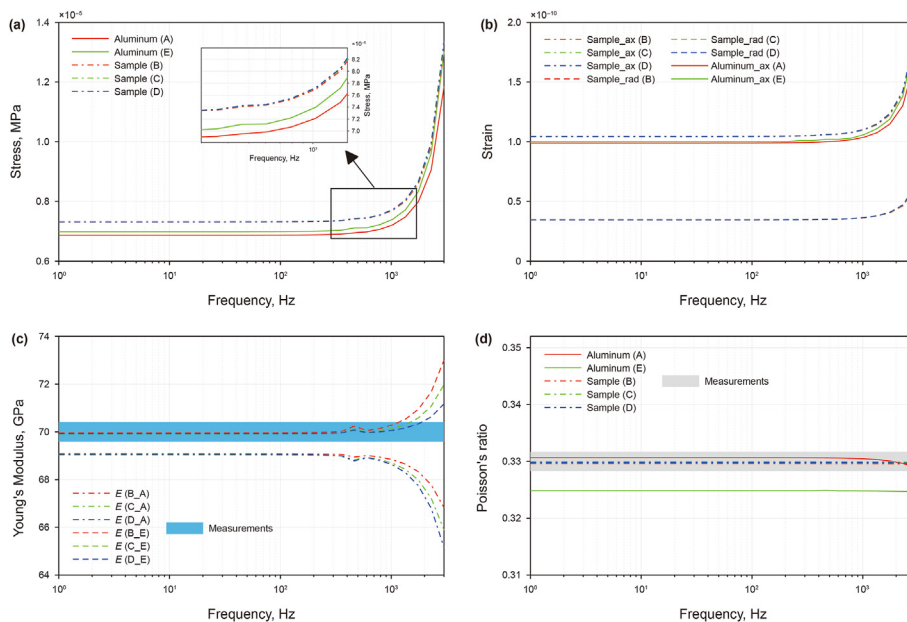


Fig. 6. Numerically simulated frequency-dependent (a) stress and (b) strain at five reference positions in the column assemblage shown in Fig. 5. The (c) Young's modulus E of the standard aluminum sample and (d) Poisson's ratio ν at five positions, inferred from the simulated stress and strain over a wide frequency range of $f \in [1-3000]$ Hz, are compared with the E and ν measurements on the same sample of diameter $D = 38.1$ mm, length $L = 75.6$ mm, Young's modulus $E = 70$ GPa, and Poisson's ratio $\nu = 0.33$.

the aluminum endplate. We mention here again that the simulated results, as well as the experimental measurements, are based on the recorded signals using the strain gauges occupying a very localized region (1×5 mm) of the sample. Although the strain gauges may precisely measure the point elastic properties of the homogeneous media, these obtained local measurements may not be representative of the entire sample in the case of an inhomogeneous media. Nevertheless, the numerical simulation suggests that the Young's modulus and Poisson's ratio have negligible deviations with respect to the experimentally measured values for the aluminum sample at normal frequencies, although the broad-frequency-band laboratory module will inevitably be affected by resonant frequencies above 2000 Hz.

4. Laboratory results on the dispersion of elastic waves in porous rock samples

The frequency and pressure dependence of the two main parameters, Young's modulus E_{LF} and Poisson's ratio ν_{LF} , have been investigated for two sets of shale and sandstone samples.

4.1. Frequency dependence of the dry shale sample's elastic properties

An as-received L shale cores, used in the experiments, were assumed to be transverse isotropic (TI) (e.g., Han et al., 2020; Chen et al., 2023). Laboratory experiments similar to the procedure described for the calibration with three standard samples were carried out on three differently oriented (0° , 45° and 90° with

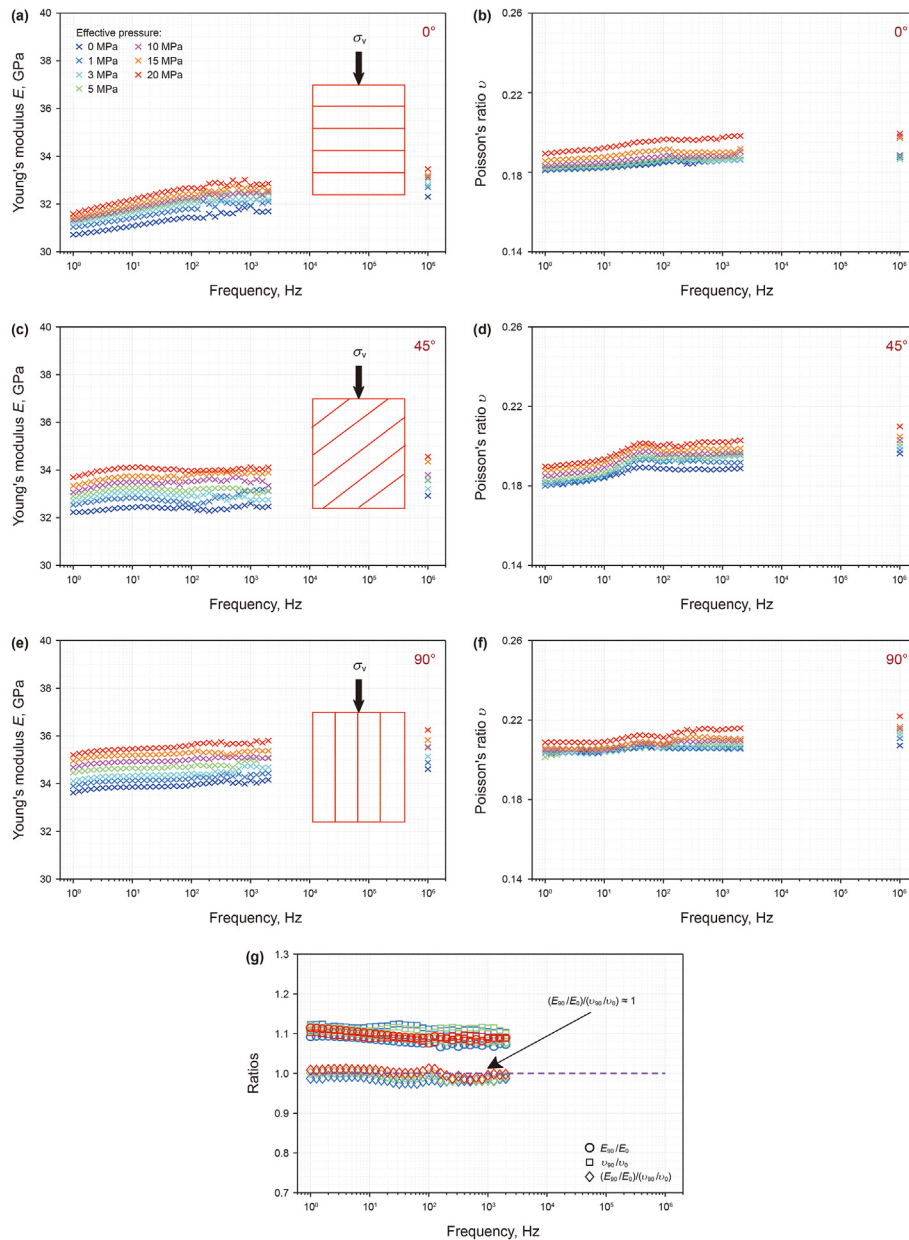


Fig. 7. Laboratory measured frequency dependence of (a, c, and e) the Young's modulus E_{LF} and (b, d, and f) the Poisson's ratio ν_{LF} (\times symbols) for the 0° , 45° and 90° oriented L shale core plugs exposed to seven different confining pressures: 0 MPa, 1 MPa, 3 MPa, 5 MPa, 10 MPa, 15 MPa, and 20 MPa. The deduced seismic $(E_{90}/E_0)/(\nu_{90}/\nu_0)$ for TI symmetry is illustrated in (g). Low frequency results were measured directly, while ultrasonic values were determined with the use of the measured directional P- and S-wave velocities.

respect to the symmetry axis) shale samples. These core plugs from the same batch of material have a very low porosity, and a series of experimental measurements were carried out in which pressure and fluid effects on seismic dispersion were investigated. In this presented work, only some selected measurements on moist (i.e., room-dry) shale samples are summarized in Fig. 7, in order to testify the measuring capabilities of the new experimental apparatus. Note the laboratory experiments were performed without any pore pressure regulation, and a constant axial stress of ~0.3 MPa was loaded on the core plug to maintain an improved signal quality for the stress-strain measurements.

Fig. 7 shows the measured directional Young's moduli E_{LF} and Poisson's ratios ν_{LF} on the L shale core plugs having three different orientations at low and ultrasonic frequencies and under different confining pressures. The corresponding ultrasonic values were determined with the use of the measured directional P- and S-wave velocities. We see from Fig. 7a, 7c and 7(e) that the 0°-orientated sample possesses slightly apparent dispersion in Young's modulus, compared with the measurements on 45°- and 90°-orientated samples. It appears that directional Poisson's ratios in Fig. 7b and 7d have negligible frequency dependence, while measurements in the 45°-orientated sample in 7f possess sizeable dispersion at the low frequencies between 1 and 50 Hz. Note that the Young's moduli and Poisson's ratios at ultrasonic frequency are slightly larger than their measurements at low frequencies. We observe clearly that the stress sensitivity of measured Young's moduli and Poisson's ratios are different. While the Young's moduli increase with increasing pressure in three samples, the measured Poisson's ratios are less sensitive to the confining pressure variations at seismic and ultrasonic frequencies for uniaxial loading. As the confining pressure increases from 0 MPa to 20 MPa for instance, the Young's modulus increases from 32.2 GPa to 34.3 GPa by ~6.5% for the 45° oriented core at frequency $f = 20$ Hz, the Poisson's ratio increases from 0.187 to 0.193 by ~3.2%. It is also interesting to find that for three core plugs, the changes in Young's modulus are similar at low seismic and high ultrasonic frequencies.

The measurement results in Fig. 7 also illustrate features that are characteristic for the transversely isotropic (TI) materials: (I) the vertical Young's modulus obtained with the 0° sample, E_0 , is distinctly smaller than the horizontal one loading parallel to bedding plane, E_{90} ; (II) the Young's modulus for the 45° sample, E_{45} , lies in between measurements obtained with 0° and 90° samples, i.e., $E_0 < E_{45} < E_{90}$; and (III) the measurements satisfy the symmetry of TI rocks described as (e.g., Szewczyk et al., 2016)

$$\frac{\nu_0(\omega)}{E_0(\omega)} = \frac{\nu_{90}(\omega)}{E_{90}(\omega)}, \quad (15)$$

where $\nu_0(\omega)$ and $\nu_{90}(\omega)$ are Poisson's ratio measured from the 0° and 90° samples, respectively. As indicated in Fig. 7g, it seems that $(E_{90}(\omega)/E_0(\omega))/(\nu_{90}(\omega)/\nu_0(\omega)) \approx 1$ is independent of frequency within the tolerant experimental errors, indicating that L shale can be considered as transversely isotropic rocks. And this further provides us confidence in the capability of measuring pressure induced changes in Young's modulus and Poisson's ratio using the new laboratory device. The experimental measurements will be further described and physical interpretations will be provided in more details in our forthcoming publications.

4.2. Effect of fluid and pressure on sandstone sample's elastic moduli

The detailed experimental procedures are then tested on the tight sandstone sample under dry-, brine- and glycerin-saturated conditions, to demonstrate how the fluid and pressure changes

influence the rock's evolution of the frequency dependence of Young's modulus, Poisson's ratio and their corresponding attenuation.

4.2.1. Tight sandstone sample

For the low-porosity and low-permeability tight sandstone investigated in this study, the pore microstructure may have a significant role on dynamic elastic behaviors than the porosity (e.g., Subramaniyan et al., 2015; Yin et al., 2017). While the cylindrical core plug of 38.1 mm in diameter and 75.2 mm long is similar to that used in He et al. (2021), its permeability is about 1 order-of-magnitude lower. As qualitatively illustrated from the thin section photomicrograph and SEM image of the original core plugs in Fig. 8, the selected rock, whose approximate mineral contents are summarized in Table 1, exhibits a relatively compact and random grain orientation and is well sorted. From the thin section image in Fig. 8a, different colors indicate different minerals and pores. The white and dark areas represent quartz and pores, respectively, while the yellow region represent the cement. Especially, the rock sample used in this study possesses, respectively, mineral size ranging from around 120 μm up to 250 μm and pore size ranging from about 100 μm to 180 μm , which are small compared with the used strain gauges of 5 mm length. Thus, the core sample can be considered isotropic and homogeneous at the REV scale (i.e., volume \gg volume of grains), and hence allowing for a good application of the forced-oscillation technique tested in this study. Moreover, the section SEM image (Fig. 8b) shows that the rock's pore microstructure is complicated and consists of couple different kinds of pores and cracks with varied size and shape. From this thin section, the estimated pore-throat size of the tight sandstone sample is mainly around 0.3–4.2 μm , and this reveals that the pore geometry of this tight core sample possesses a possible porous-cracked microstructure.

4.2.2. Laboratory measurements on pressure and frequency dependence of elastic moduli in saturated sample

In Fig. 9, the pressure dependence of Young's modulus E_{LF} and Poisson's ratio ν_{LF} , as well as their corresponding attenuation (or inverse quality) $1/Q_E$ and $1/Q_\nu$, respectively, which were obtained via the stress-strain technique at 1–2000 Hz and using ultrasonic method at 1 MHz, is reported for the core sample under dry or nitrogen gas saturated condition. It is indeed expected that there has negligible frequency dependency in the experimental measurements at each confining pressure. For measured E_{LF} (Fig. 9a) and ν_{LF} (Fig. 9a), however, a distinct dependence to confining pressure can be observed. Consistently, within the measured frequency range of $f \in [1-2000, 10^6]$ Hz, an increase in both E_{LF} and ν_{LF} , from 15 GPa to 20 GPa and from 0.08 to 0.16, respectively, were measured with an increasing value of effective pressure P_{eff} from 0 MPa to 20 MPa. It seems that these strong pressure dependencies obtained on Young's modulus and Poisson's ratio may be attributed to a significant variation in the rock's compliant pores. According to previous studies (e.g., see Pimienta et al., 2015; Spencer and Shine, 2016; Yin et al., 2017), the measured dry E_{LF} and ν_{LF} are expected to increase with increasing P_{eff} for homogeneously isotropic rocks. The exerted confining pressure P_C increase causes gradual closure of the horizontal compliant porosity or microcracks with small aspect ratio, thus strengthening the rock stiffness. Moreover, the corresponding attenuation, $1/Q_E$ and $1/Q_\nu$, are small and exhibit weak pressure dependence.

The frequency dependence of elastic moduli, measured on the tight sandstone core saturated by brine, is demonstrated in Fig. 10. Large frequency-dependent variations of E_{LF} and ν_{LF} , as well as $1/Q_E$ and $1/Q_\nu$, are observed. As the bulk modulus of low-compressibility pore fluid increases, the measured E_{LF} and ν_{LF} , significantly increase

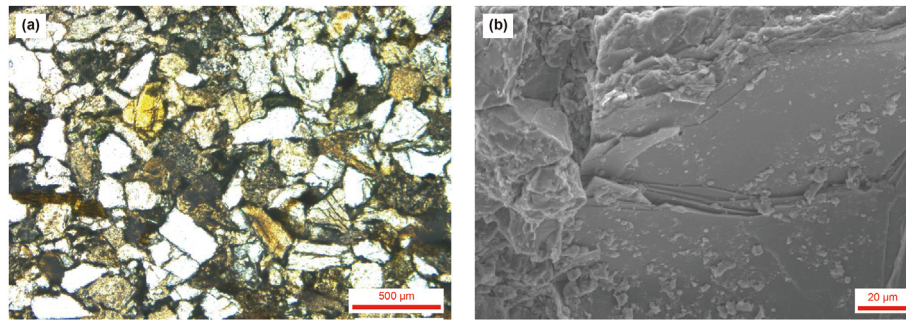


Fig. 8. Microscopic image of a thin section of the tight sandstone with parallel light showing a cross section of the core sample (a), and scanning electron microscopy (SEM) images of a thin section of the sandstone (b).

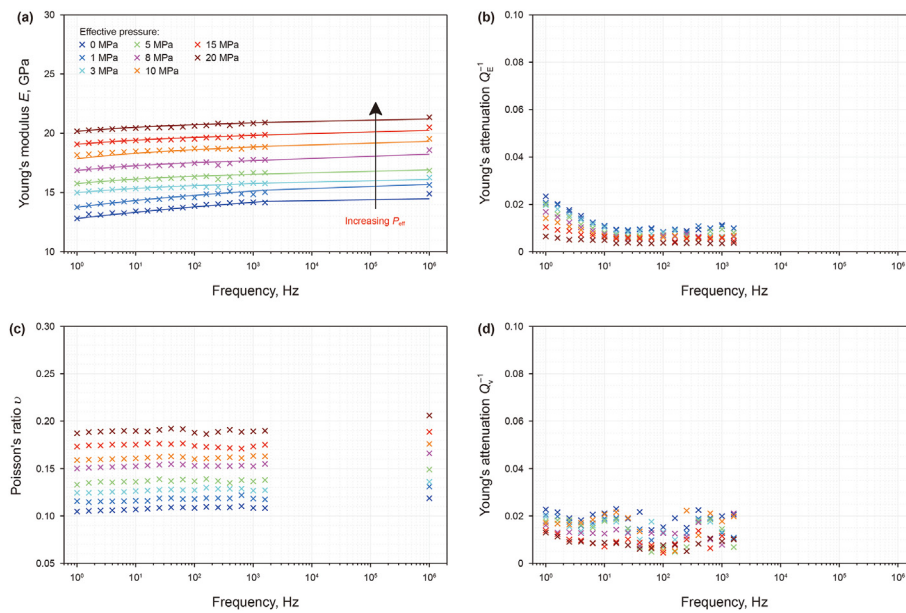


Fig. 9. Demonstrations of the applications of the modified experimental apparatus for seismic dispersion and attenuation measurements: measured frequency dependence of the Young's modulus E_{LF} and Poisson's ratio ν_{LF} and the corresponding attenuation $1/Q_E$ and $1/Q_\nu$ for the tight sandstone saturated with nitrogen gas at different effective pressures. The core sample was investigated at the air conditioning of the room temperature, during isotropic loading with atmospheric pore pressure. Solid curves in (a) show a parametric fit to the experimental measurements based on the Kramers-Kronig relationship (e.g., Mikhaltsevitch et al., 2016b).

with respect to the dry case. It is also interesting to notice that at effective pressure P_{eff} higher than 8 MPa, E_{LF} exhibits negligible frequency dependence at frequencies $f = [1-2000]$ Hz. It appears that the value of E_{LF} increases with the increasing effective pressure as the dry rock measurements, while ν_{LF} is reversely correlated as effective pressure increases and all measured results converge to a ν_{LF} level around 0.23. This reveals that the effective pressure strongly damps the differences in Poisson's ratio between the dry and fluid-saturated core sample. Here, $1/Q_E$ and $1/Q_\nu$ decrease with increasing effective pressure over the measured frequencies. For a given effective pressure P_{eff} , we find that $1/Q_E$ (Fig. 10b) increases when frequency increases; on the contrary, $1/Q_\nu$ decreases with the increasing frequency (Fig. 10d). Furthermore, it seems that the $1/Q_E$ peak has a maximum at round $f \approx 80$ Hz for all effective pressures.

For the tight sandstone under glycerin saturation (Fig. 11), we observe strong frequency dependence of elastic moduli and the associated attenuation. As the frequency increases from 1 to 2000 Hz, at a given effective pressure $P_{eff} = 3$ MPa, the measured E_{LF} increases significantly from ~ 25 GPa to ~ 34 GPa by 36%, while a continuous increase in ν_{LF} from ~ 0.23 to ~ 0.28 by 21.7% is discovered. Overall, with increasing frequency, ν_{LF} gradually increases up

to a magnitude close to the value deduced from the measured ultrasonic velocities using Eq. (2). We notice that the frequency-dependent $1/Q_E$ decreases when increasing P_{eff} , which is consistent with the fact that the horizontal small aspect ratio microcracks gradually close as the effective pressure increases. In particular, a high attenuation peak of approximately $1/Q_E = 0.09$, is extracted from the measurements for about $f = 11$ Hz and at the lowest effective pressure $P_{eff} = 0$ MPa. As reported in Yin et al. (2017), the peak of $1/Q_E$ is moved to higher frequencies due to the temperature increase caused decrease in viscosity of glycerin. The experimental measurements were carried out at a temperature around $T = 23$ °C, which may account for the low characteristic frequency measured in the peak that was highly fluid viscosity dependent. We also find that the pressure-dependent $1/Q_\nu$ peak possesses the nearly identical characteristic frequency (i.e., $f \approx 11$ Hz) with $1/Q_E$. Furthermore, it seems that the characteristic frequency corresponding to the attenuation peak was not strongly affected by effective pressure and fluid viscosity for this specific sandstone.

The pressure-dependent increase of E_{LF} results under different fluid saturation, in Figs. 9a, 10a and 11a, show that the Young's moduli computed using KKR are in a good agreement with the

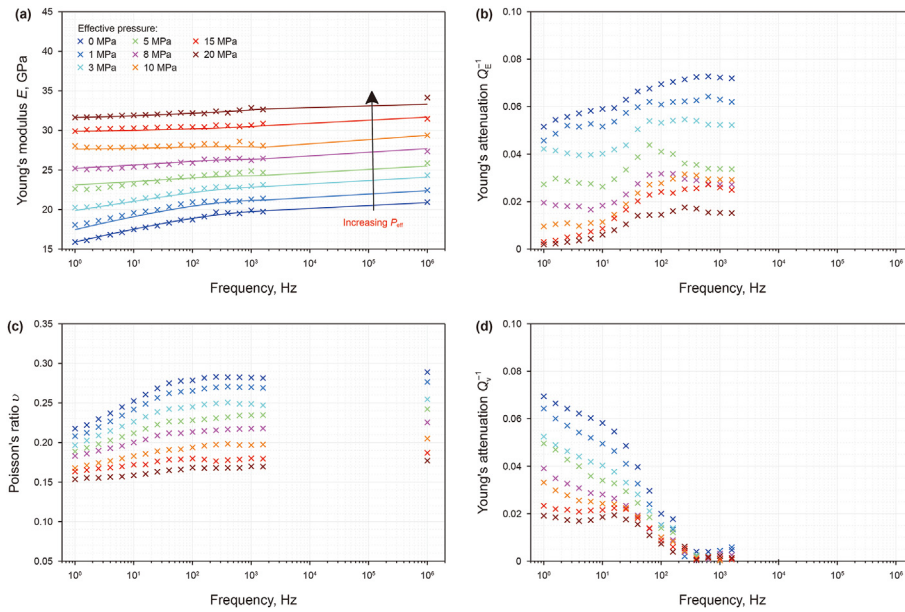


Fig. 10. Demonstrations of the applications of the modified experimental apparatus for seismic dispersion and attenuation measurements: measured frequency dependence of the Young's modulus E_{LF} and Poisson's ratio ν_{LF} and the corresponding attenuation $1/Q_E$ and $1/Q_V$ for the tight sandstone saturated with brine at different effective pressures. The core sample was investigated at the air conditioning of the room temperature, during isotropic loading with atmospheric pore pressure. Solid curves in (a) show a parametric fit to the experimental measurements based on the Kramers-Kronig relationship (e.g., Mikhaltsevitch et al., 2016b).

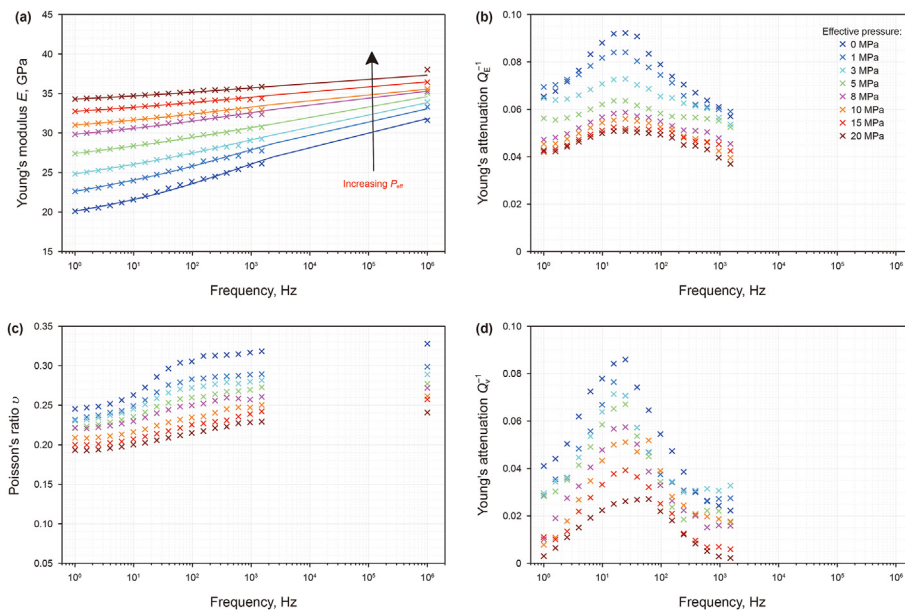


Fig. 11. Demonstrations of the applications of the modified experimental apparatus for seismic dispersion and attenuation measurements: measured frequency dependence of the Young's modulus E_{LF} and Poisson's ratio ν_{LF} and the corresponding attenuation $1/Q_E$ and $1/Q_V$ for the tight sandstone saturated with glycerin at different effective pressures. The core sample was investigated at the air conditioning of the room temperature, during isotropic loading with atmospheric pore pressure. Solid curves in (a) show a parametric fit to the experimental measurements based on the Kramers-Kronig relationship (e.g., Mikhaltsevitch et al., 2016b).

laboratory measurements. This illustrates that the modulus dispersion and attenuation measurements are consistent with the causality principle and can faithfully represent the intrinsic properties of the considered sample. Thus, we conclude here that our experimental data on the tight sandstone of dry, brine-saturated and glycerin-saturated conditions demonstrate that the new laboratory module is reliable and can be employed to precisely extract modulus dispersion and attenuation for viscoelastic media. In a short summary, dispersion in the measured Young's modulus and

Poisson's ratio, as well as their associated attenuation, are almost negligible for the N_2 saturated core. However, observable frequency dependence was found for the tight sandstone filled with brine or glycerin under different effective pressures. Measured Young's moduli of the sandstone with brine saturation are significantly larger than those with gas saturation, but smaller compared to the glycerin saturation case. The measured results exhibit the declining tendency of dispersion and attenuation with increasing pressure. Furthermore, the estimated characteristic frequency of glycerin

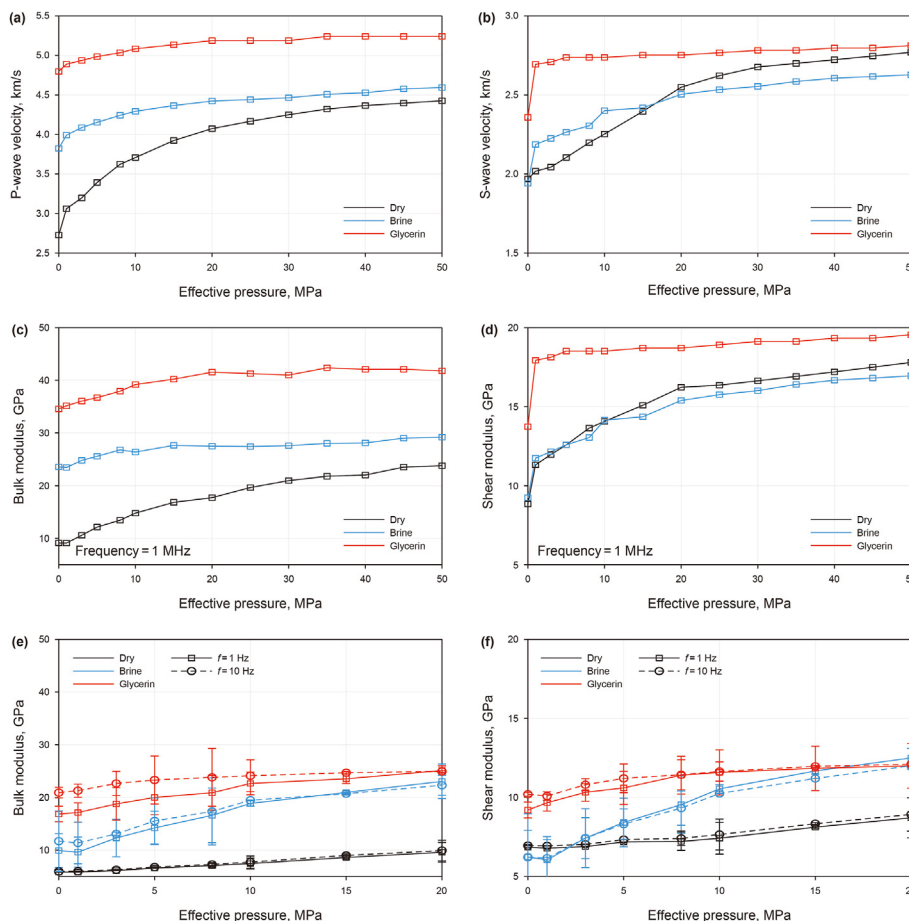


Fig. 12. Laboratory elastic measurements for the tight sandstone sample under dry, brine and glycerin saturation conditions, as a function of effective pressure. (a) and (b) represent P- and S-wave velocities at ultrasonic frequency of 1 MHz, and (c) and (d) represent high-frequency bulk and shear moduli calculated from elastic wave ultrasonic velocity measurements. (e) and (f) are the mean results for bulk and shear moduli and their standard error bars at low frequencies of 1 and 10 Hz, using the seismic elastic moduli measurement system for oscillation of confining pressure. At these frequencies, bulk and shear moduli are significantly affected by pore fluid. The frequency effect is apparently demonstrated.

saturated sample is shifted towards lower frequencies compared to the brine saturated sample, in agreement with potential influence for declined fluid viscosity.

In Fig. 12, the pressure and pore fluid dependences of bulk modulus K and shear modulus μ on tight sandstone is presented for two measuring low frequencies of $f = [1; 10]$ Hz using Eq. (8), as well as the ultrasonic frequency $f = 1$ MHz using Eq. (2). The K and μ measurements under dry conditions are compared with the values under glycerin and water saturations. Overall, the pressure dependence is very large for both elastic moduli. For ultrasonic velocity measurements (Fig. 12a and 12b), increasing pressure leads to increased P- and S-wave velocities, as well as the bulk and shear moduli. It is therefore likely that the contained numerous micro-cracks in the test sample progressively close during pressurization cycle. We find that the P- and S-wave velocities reach a plateau at the high pressure, at which the experimental measurements should faithfully represent the elastic characteristics of the background matrix and the non-closeable pores. Both P- and S-wave velocities, as well as the extracted E_{HF} and μ_{HF} (Fig. 12c and 12d), exhibit strong sensitivities to variations in the bulk modulus of pore fluid (see Table 2). As the pore fluid bulk modulus increases, we find the high-frequency P-wave velocity shows higher magnitude and less pressure dependence. Different with that, an increase in the bulk modulus of pore fluid caused the S-wave velocity to exhibit higher magnitude at low pressures only. At the intermediate

pressures of $P_{eff} \approx 18$ MPa for this specific core sample, there has an obvious “crossing point” between the dry and brine-saturated S-wave velocities, after which brine-saturated S-wave velocities take lower values than the dry ones. Overall, the measured “crossing point” corresponds to the point at which the acoustic characteristics become affected strongly by non-closable pores. It is important to note that these observations were reported by numerous researchers on many sandstones and other kinds of rocks (e.g., David et al., 2013; Yin et al., 2017).

Measured results of low-frequency bulk and shear moduli, obtained from the axial stress oscillation at two frequencies, are presented in Fig. 12e and 12f, respectively. It appears that at each effective pressure, the dry, glycerin- and brine-saturated low-frequency bulk and shear moduli present significant deviations. It is as expected that the dry sample has the lowest value of low-frequency bulk modulus, while bulk modulus of the brine-saturated sample lies in between the values of the dry and glycerin saturation cases (Fig. 12e). Interestingly, two “crossover point”, at low and high pressures, respectively, are observed on the measured low-frequency shear modulus of the glycerin-saturated sample (Fig. 12f). This demonstrates that an increase in the pore fluid bulk modulus results in larger μ_{LF} values at pressures higher than about 3 MPa. It is also clearly observed that μ_{HF} of brine-saturated sample is slightly smaller than the one of glycerin-saturated sample at pressures higher than about 18 MPa, which is related to the fluid’s

viscosity and the sample's overall compressibility. Please also note that the extracted elastic moduli are independent of the oscillation amplitude, considering that the exerted strain levels on the sandstone during forced oscillating tests are less than about 10^{-6} . Under glycerin or brine saturation, it was found that the obtained elastic moduli at the frequency $f = 10$ Hz possess slightly less pressure dependence than the values at $f = 1$ Hz. Here, the obvious errors on the measurements, as indicated with the error bars, may arise from the bonding of strain gauges on the samples, as well as the accuracy limit of applied strain gauges.

4.3. Interpretation of the frequency effects for the fluid-saturated tight sandstone

The strong frequency- and pressure-dependent variations in elastic moduli and attenuation measurements in fluid-saturated sandstones are often considered as a result of fluid flow at various scales which causes transitions between the various elastic regimes (e.g., Müller et al., 2010; Pimienta et al., 2016; He et al., 2023). Three main regimes investigated are separated by two characteristic frequencies, corresponding to the drained/undrained transition f_1 and the undrained (relaxed)/unrelaxed transition f_2 , respectively, can be defined as follows (e.g., Pimienta et al., 2016)

$$f_1 = \frac{4\kappa K_d}{\eta_f L^2} \quad \text{and} \quad f_2 = \frac{\alpha^3 K_d}{\eta_f}, \quad (16)$$

where η_f represents the fluid viscosity, κ represents the rock permeability, K_d represents the rock drained bulk modulus, L represents the sample's length, and α represents the characteristic frequency f_2 , associated with the pore-scale squirt flow phenomenon, relies strongly on microcrack aspect ratio α . Moreover, since both drained and undrained regimes are considered to be poroelastic and relaxed at the REV scale, the characteristic frequency f_1 cannot be higher than f_2 .

Since the poroelastic model of Biot (1956), numerous effective medium theories have been introduced to explain the fluid effect on rock's different elastic properties (e.g., Johnson, 2001; Gurevich et al., 2010; Adelinet et al., 2011; de Paula et al., 2012; Zong et al., 2022 to name just a few). Our main purpose is to examine the consistency of the experimental measurements, with the poroelastic models in the framework of fluid flow theories. The local or pore-scale squirt flow, caused by a passing wave induced unequal pore-fluid pressure between pore spaces of different shapes or compliance, is usually taken as the main mechanism for the undrained/unrelaxed transition (e.g., Rubino and Holliger, 2013). For the glycerin-saturated sandstone sample, nevertheless, the observed extensional attenuation peak does not shift towards a lower frequency with an increase of effective pressure, indicating the measured results may not be fully understood with the squirt flow phenomenon solely. Thus, a poroelastic model with the combined effects of different inter-dependent attenuation mechanisms (e.g., squirt flow mechanism and mesoscopic mechanism) may possibly help to better account for the results that we acquired for the glycerin saturation. Here, a scaled poroelastic model (SPM), similar to the model proposed in He et al. (2021) that accounts for the wave-induced fluid flow mechanisms at both microscopic and mesoscopic scales, was employed to calculate the E_{LF} and $1/Q_E$ values over the investigated frequency range.

Via combining a generalized 1D model in Müller and Gurevich (2004) of 3D random patchy saturation scale (Toms et al., 2007) with the microscopic squirt flow effects, we aim to compare the frequency dependence of laboratory measurements in the tight sandstone sample with predictions of the poroelastic model.

Experimental observations indicate that mesoscopic fluid heterogeneities of the irregular geometries and random distributions in space produce significant impacts on moduli dispersion and attenuation. On the basis of an approximation for the coherent wavefield in 3D randomly heterogeneous porous media, a continuous random model was developed to characterize seismic dispersion and attenuation when fluid patches possess complex distribution. For an exponential correlation function with a correlation size b that describes the characteristic length of heterogeneous patches, the effective complex elastic modulus can be represented as (Toms et al., 2007)

$$C(\omega) = C_0 \left(1 - \Delta_2 - \frac{\Delta_1 k^2 b^2}{(ik - b - 1)^2} \right)^2, \quad (17)$$

here $\Delta_1 = (L/H)$, $\Delta_2 = \alpha^2 M \sigma^2 / 2H$, $N = ML/H$, $k = (i\omega\eta/\kappa N)^{1/2}$, $M = [(\alpha - \varphi)/K_S + \varphi/K_F]^{-1}$, $\alpha = 1 - K^{\text{dry}}/K_S$, $L = K^{\text{dry}} + 4/3\mu$, $H = K^{\text{dry}} + 4/3\mu$, and C_0 indicates the mean elastic modulus of rock matrix. κ denotes permeability, η denotes fluid viscosity and, μ represents dry rock shear modulus. K_S and K_F are bulk moduli of solid grain and pore fluid and, K^{dry} and K^{sat} are bulk moduli of dry and saturated rocks, respectively. Therefore, the frequency-dependent P-wave phase velocity and attenuation can be obtained

$$V_P(\omega) = \sqrt{\text{Re}(C)/\rho}, \quad \text{and} \quad Q_P^{-1}(\omega) = \text{Im}(C)/\text{Re}(C). \quad (18)$$

Specially, the simple squirt model derived by Gurevich et al. (2010), which considers the influences of the crack aspect ratio and crack porosity, is practically suitable for explaining the measured results on tight sandstones having the porous-cracked microstructures. For a modified rock frame in which the stiff pores are drained whereas the compliant pores are completely fluid-saturated, partially relaxed bulk modulus K_{mf} and shear modulus μ_{mf} associated with squirt flow mechanism can be estimated as functions of frequency and pressure (Gurevich et al., 2010)

$$\frac{1}{K_{mf}(P, \omega)} = \frac{1}{K_h} + \frac{1}{\frac{1}{K_{dry}(P)} + \frac{1}{K_h}} + \frac{1}{\varphi_c(P) \left(\frac{1}{K_f^*(P, \omega)} + \frac{1}{K_m} \right)}, \quad \frac{1}{\mu_{mf}(P, \omega)} = \frac{1}{\mu_{dry}(P)} - \frac{4}{15} \left[\frac{1}{K_{dry}(P)} - \frac{1}{K_{mf}(P, \omega)} \right], \quad (19)$$

where $\varphi_c(P)$ is the compliant porosity, K_h is the bulk modulus of the dry frame for an assumptive rock where compliant pores are closed, and K_m is the mineral bulk modulus. $K_{dry}(P)$ and $\mu_{dry}(P)$ represent the bulk and shear moduli of the dry frame, respectively, inferred from the measured ultrasonic velocities. The frequency-dependent bulk modulus of a modified fluid filling the compliant pores, K_f^* , which relies on the aspect ratio α of the compliant pores and fluid viscosity η , can be defined as

$$K_f^*(P, \omega) = \left[1 - \frac{2J_1(ka)}{kaJ_0(ka)} \right] K_f, \quad (20)$$

here K_f denotes the pore fluid bulk modulus, $ka = (-3i\omega\eta/K_f)^{1/2}/\alpha$, and J_0 and J_1 denote the 0th and 1st Bessel function, respectively. Using the approach in de Paula et al. (2012), compliant porosity $\varphi_c(P)$ and stiff porosity $\varphi_s(P)$ (i.e., $\varphi = \varphi_s + \varphi_c$) are obtained from the pressure dependency of dry ultrasonic measurements of the compressional and shear velocities. Through simply incorporating the frequency-dependent moduli of the modified dry frame (Eq.

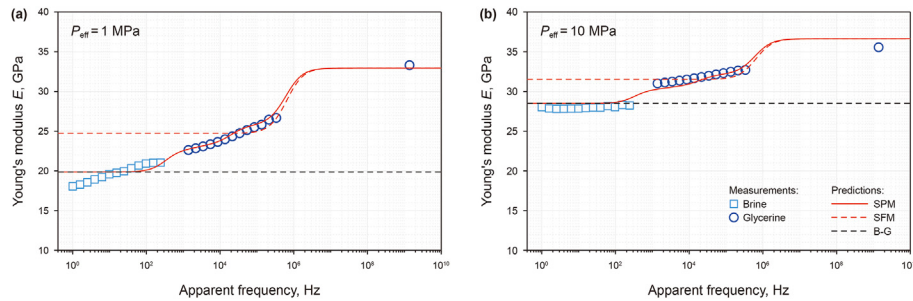


Fig. 13. Laboratory experimental measurements of Young's modulus E as a function of apparent frequency f_c (Eq. (21)) for the tight sandstone saturated with brine (squares) and glycerin (circles) at two effective pressures of (a) 1 MPa and (b) 10 MPa. The measured results are compared with the corresponding predictions from the squirt flow model (dashed red curves) and the scaled poroelastic model (solid red curves) that considers microscopic and mesoscopic fluid flow effects. In addition, the undrained E is obtained from the drained modulus using the Biot-Gassmann (B-G) equation and is plotted as the dashed black curve. The measured results displayed here represent a selection of data illustrated in Figs. 10a and 11a.

(19) into the 3D random porous media (Eq. (17)), the scaled poroelastic model is able to help understand the combined influences of fluid flows at both microscopic and mesoscopic scales on elastic moduli and the associated attenuation of the saturated tight sandstone.

In Fig. 13, the laboratory measured and the predicted Young's modulus E for the brine- and glycerin-saturated tight sandstone under two effective pressures of 1 and 10 MPa are compared. Note the measured results are plotted as a function of apparent frequency f_c , which is a key parameter allows accounting for the fluid's viscosity η_f effect on the corresponding scaled values in a broad frequency range and is defined as (e.g., Pimienta et al., 2015; Spencer and Shine, 2016; Yin et al., 2017)

$$f_c = f^* \frac{\eta_f}{\eta_0}, \quad (21)$$

with η_0 denoting viscosity of brine and $f \in [1-2000, 10^6]$ Hz denoting the measurement frequency. Thus, the apparent frequency for glycerin can be obtained $f_c = 1379 * f \in [1.4 \times 10^3 - 2.8 \times 10^5, 1.4 \times 10^9]$ Hz, assuming the *in situ* brine viscosity $\eta_0 = 1.0226 * 10^{-3}$ Pa s. Here, the characteristic patch scale was assumed to be $b = 18$ mm. Compliant porosity and aspect ratio of $\varphi_c = 0.00002$ and $\alpha = 0.0001$, respectively, are extracted and employed for the squirt flow modelling.

In general, it appears that the predicted Young's modulus E from the squirt flow model (SFM) show the similar overall behaviors as the laboratory measurements, while the ones from the SPM are in a reasonably good fit with the experimental results. Thus, it is likely that the combined mesoscopic and microscopic flow mechanisms are responsible for the measured dispersion. Note further that the predicted E of glycerin saturation remains constant at frequencies beyond 2×10^6 Hz. For glycerin saturation, owing to the influence of fluid flow mechanism at mesoscopic scale, it seems that the E prediction using the SPM is significantly below the one using the SFM at frequencies low than 3×10^4 Hz. Moreover, we observed that the SPM prediction properly fits the data frequency dependence at the low-frequency measurements, but it underestimates it in the case of ultrasonic measurements. In addition, although the SPM predicted Young's modulus is well consistent with the measured E under brine-saturated condition at effective pressure of 10 MPa, it deviates from it in the case of an effective pressure of 1 MPa. This indicates that the measured frequency dependence is more spread out than expected in the case of a unique frequency influence, and hence implying the possible intrinsic viscoelastic effect of the clay content and the influences of heterogeneous distributions of the aspect ratios of microcracks, as well as the microcrack density, in the tight sandstone sample. Therefore, future

efforts are required to develop a theoretical model that can be used to more accurately account for the measured frequency dependence.

5. Discussions

A new laboratory apparatus allowing for combined measurements of elastic properties at high frequency and at low frequency under various confining pressure conditions was described in this presented work. The following arguments might arise considering the experimental apparatus and procedure and the interpretation of measured results. First, to better evaluate its measuring accuracy and capability, three standard samples (i.e., aluminum, titanium and lucite) were utilized to calibrate the experimental apparatus. The results illustrate that for axial strain magnitudes as low as 10^{-6} , reliable measurements can be obtained at frequency range of $f \in [1-2000]$ Hz, using the same strain gauges with higher gauges factors and resistance provided by the manufacturer. It should be noted that the observed strain amplitudes may be strongly affected by the resistance deviations up to 10%, resulting in magnified errors in experimental measurements. A major drawback of the stress-strain technique employed here to obtain seismic dispersion and attenuation is that the measurements at oscillating frequencies lower than 1 Hz cannot be reliably performed because of the applied actuator which may not continuously generate stable mechanical stress at very low frequencies condition.

In addition, reduction of experimental errors and consistent results in modulus dispersion and attenuation can be obtained for isotropic homogeneous samples. It should also be noted that the introduced experimental technique relying on the local moduli measurements is dependent on the degree of fluid saturation and the distribution of fluid phase, and also the frequency dependence of the measured elastic moduli seems to be affected significantly by these factors, as argued by others (e.g., Mikhaltsevitch et al., 2016a; Li et al., 2019). Although the fluid injection procedure in the SEM, which is one of the most commonly used ways to conduct fluid displacement during experiments, can regulate the fluid injection rate, it is very difficult to ascertain either a perfectly homogeneous distribution of concerned fluid or a complete saturation due to the existing capillary force effects at microscopic scale that might affect the effective bulk moduli of pore fluid and also possibly the rock stiffness.

Furthermore, laboratory ultrasonic measurements are sometimes performed as part of time-lapse seismic monitoring of reservoir and overburden performance during fluid depletion and/or injection. Taking no account of the frequency dependence of elastic moduli, in case of fluid-saturated sandstone, however,

people may come up with a conclusion that time-lapse seismic attributes (e.g., time shifts and amplitude differences) related to the expected elastic property variations in the field would be too weak to be identified. Nevertheless, in reality, 4D seismic attributes could be well detected owing to the enhanced elastic moduli within seismic frequencies. This again highlights the significance of experimental measurements, especially for those carries out at the low seismic frequency range.

Finally, although the theoretically calculated data can fairly well reproduce the measured frequency dependence of the Young's modulus from the fluid-saturated tight sandstone sample at low frequencies and at two low effective pressures, the calculated deviations from experimental results indicate that the effects of porosity change with pressure, microstructure heterogeneity, and microcrack density and distribution, as well as additional fluid flow mechanism, should be considered. Future work will focus on understanding the source and nature of the measured dispersion and attenuation behaviors and how to model them, especially for partially fluid saturation conditions.

6. Conclusion

We introduce a new experimental system to investigate the pressure and fluid effect on the elastic moduli dispersion and attenuation at low seismic and ultrasonic frequencies on natural cored porous rocks. Calibration measurements of the forced oscillation device have been successfully carried out with aluminum, titanium and lucite samples at room temperature condition, demonstrating that the SEMM can perform stably in the effective pressure and frequency ranges of $P_c \in [0-40]$ MPa and $f \in [1-2000, 10^6]$ Hz, respectively. A numerical model was also employed to assess the dynamic limits of the device, revealing that the induced axial and radial strain amplitudes were not affected by the strain gauges' position for the standard aluminum sample. Moreover, two sets of laboratory measurements using axial stress oscillations were designed on shale and tight sandstone samples, based on the experimental procedures, to explore the influences related to anisotropy, pressure and fluid on frequency-dependent elastic parameters. It was found that the measured Young's modulus and Poisson's ratio, for the humidified core samples, show negligible dispersion as expected. Nevertheless, we observe that the measured Young's modulus E_{LF} and Poisson's ratio ν_{LF} , as well as the corresponding attenuation $1/Q_E$ and $1/Q_V$, on the tight sandstone saturated with glycerin at various effective pressures possess different frequency dependence, compared with those results on the brine saturation case. Our analysis of the Young's modulus dispersion measurements on the fluid-saturated sandstone illustrates that elastic modulus dispersion is possibly dependent on the combined fluid flow mechanisms at mesoscopic and microscopic scales, although the heterogeneous aspect ratio distributions of microcracks of the core may also play a significant role on controlling the observed elastic parameters.

Acknowledgements

The authors would like to acknowledge financial support from NSFC Basic Research Program on Deep Petroleum Resource Accumulation and Key Engineering Technologies (U19B6003-04-03), National Natural Science Foundation of China (41930425), Beijing Natural Science Foundation (8222073), R&D Department of China National Petroleum Corporation (Investigations on fundamental experiments and advanced theoretical methods in geophysical prospecting applications, 2022DQ0604-01), Scientific Research and Technology Development Project of PetroChina (2021DJ1206) and National Key Research and Development Program of China (2018YFA0702504).

References

- Adam, L., Batzle, M., Lewallen, K.T., van Wijk, K., 2009. Seismic wave attenuation in carbonates. *J. Geophys. Res.* 114, B06208. <https://doi.org/10.1029/2008JB005890>.
- Adelinet, M., Fortin, J., Gueguen, Y., 2011. Dispersion of elastic moduli in a porous-cracked rock. *Tectonophysics* 503, 173–181. <https://doi.org/10.1016/j.tecto.2010.10.012>.
- Batzle, M.L., Han, D.H., Hofmann, R., 2006. Fluid mobility and frequency-dependent seismic velocity - direct measurement. *Geophysics* 71, N1–N9. <https://doi.org/10.1190/1.2159053>.
- Biot, M.A., 1956. Theory of propagation of elastic waves in fluid-saturated porous solid. I. Low-frequency range. *J. Acoust. Soc. Am.* 28, 168–178. <https://doi.org/10.1121/1.1908239>.
- Borgomano, J.V.M., Gallagher, A., Sun, C., Fortin, J., 2020. An apparatus to measure elastic dispersion and attenuation using hydrostatic- and axial-stress oscillations under undrained conditions. *Rev. Sci. Instrum.* 91, 034502. <https://doi.org/10.1063/1.5136329>.
- Chapman, S., Borgomano, J.V.M., Yin, H., Fortin, J., Quintal, B., 2019. Forced oscillation measurements of seismic wave attenuation and stiffness moduli dispersion in glycerine-saturated Berea sandstone. *Geophys. Prospect.* 67, 956–968. <https://doi.org/10.1111/1365-2478.12710>.
- Chapman, S., Tisato, N., Quintal, B., Holliger, K., 2016. Seismic attenuation partially saturated Berea sandstone submitted to a range of confining pressures. *J. Geophys. Res. Solid Earth* 121, 1664–1676. <https://doi.org/10.1002/2015JB012575>.
- Chen, F.B., Zong, Z.Y., Yin, X.Y., 2022. Acoustothermoelasticity for joint effects of stress and thermal fields on wave dispersion and attenuation. *J. Geophys. Res. Solid Earth* 127 (4), e2021JB023671. <https://doi.org/10.1029/2021JB023671>.
- Chen, F.B., Zong, Z.Y., Stovas, A., Yin, X.Y., 2023. Wave reflection and transmission coefficients for layered transversely isotropic media with vertical symmetry axis under initial stress. *Geophys. J. Int.* 233 (3), 1580–1595. <https://doi.org/10.1093/gji/ggad011>.
- Cole, K.S., Cole, R.H., 1941. Dispersion and absorption in dielectrics I. Alternating current characteristics. *J. Chem. Phys.* 9, 1709–1721. <https://doi.org/10.1063/1.1750906>.
- David, E.C., Forin, J., Schubnel, A., Guéguen, Y., Zimmerman, W., 2013. Laboratory measurement of low- and high-frequency elastic moduli in Fontainebleau sandstone. *Geophysics* 78, D369–D379. <https://doi.org/10.1190/geo2013-0070.1>.
- de Paula, O.B., Pervukhina, M., Makarynska, D., Gurevich, B., 2012. Modeling squirt dispersion and attenuation in fluid-saturated rocks using pressure dependency of dry ultrasonic velocities. *Geophysics* 77 (3), WA157–WA168. <https://doi.org/10.1190/geo2011-0253.1>.
- Gordon, R.B., Davis, L.A., 2012. Velocity and attenuation of seismic waves in imperfectly elastic rock. *J. Geophys. Res.* 73, 3917–3935. <https://doi.org/10.1029/jb073i012p03917>.
- Gurevich, B., Makarynska, D., Paula, O.B., Pervukhina, M., 2010. A simple model for squirt-flow dispersion and attenuation in fluid-saturated granular rocks. *Geophysics* 75, N109–N120. <https://doi.org/10.1190/1.3509782>.
- Han, T.C., Gurevich, B., Fu, L.Y., Qi, Q.M., Wei, J.X., Chen, X.Y., 2020. Combined effects of pressure and water saturation on the seismic anisotropy in artificial porous sandstone with aligned fractures. *J. Geophys. Res.* 125, e2019JB019091. <https://doi.org/10.1029/2019JB019091>.
- Harris, J., Quan, Y., Xu, C., 2005. Differential Acoustical Resonance Spectroscopy: an Experimental Method for Estimating Acoustic Attenuation of Porous Media. *SEG Technical Program Expanded*, pp. 1569–1572. <https://doi.org/10.1190/1.2147992>. Abstracts.
- He, Y.-X., He, W.T., Zhang, M.F., Zhang, J.L., Liu, W.H., Ma, X.Y., Tang, G.Y., Wang, S.X., Li, G.F., Liu, J.Z., Song, X.L., 2023. Sensitivity of seismic attenuation and dispersion to dynamic elastic interactions of connected fractures: quasi-static finite element modeling study. *Petrol. Sci.* 20, 177–198. <https://doi.org/10.1190/1.2147992>.
- He, Y.-X., Wang, S.X., Sun, C., Tang, G.Y., Zhu, W., 2021. Analysis of the frequency-dependent characteristics of wave attenuation and velocity dispersion using a poroelastic model with mesoscopic and microscopic heterogeneities. *Geophys. Prospect.* 69 (6), 1260–1281. <https://doi.org/10.1080/08123985.2020.1767504>.
- He, Y.-X., Wang, S.X., Xi, B., Tang, G.Y., Yin, H.J., Zhao, L.M., Sun, C., Ma, X.Y., 2022. Role of pressure and pore microstructure on seismic attenuation and dispersion of fluid-saturated rocks: laboratory experiments and theoretical modelling. *Geophys. J. Int.* 231 (3), 1917–1937. <https://doi.org/10.1093/gji/ggac286>.
- Huang, Q., Han, D., Li, H., 2015. Laboratory measurement of dispersion and attenuation in the seismic frequency. In: 85th Annual International Meeting, SEG. <https://doi.org/10.1190/segam2015-5909141.1>. Expanded Abstracts 3090–3094.
- Jackson, I., Paterson, M., 1987. Shear modulus and internal friction of calcite rocks at seismic frequencies: pressure, frequency and grain size dependence. *Phys. Earth Planet. In.* 45, 349–367. [https://doi.org/10.1016/0031-9201\(87\)90042-2](https://doi.org/10.1016/0031-9201(87)90042-2).
- Jackson, I., Schijns, H., Schmitt, D.R., Mu, J., Delmenico, A., 2011. A versatile facility for laboratory studies of viscoelastic and poroelastic behavior of rocks. *Rev. Sci. Instrum.* 82, 064501.
- Johnson, D.L., 2001. Theory of frequency dependent acoustics in patchy-saturated porous media. *J. Acoust. Soc. Am.* 110 (2), 682–694. <https://doi.org/10.1063/1.3592154>.
- Li, H., Wang, D.X., Gao, J.H., Zhang, M.B., Wang, Y.R., Zhao, L.X., Yang, Z.F., 2019. Role

- of saturation on elastic dispersion and attenuation of tight rocks: an experimental study. *J. Geophys. Res.* 123, e2019JB018513. <https://doi.org/10.1029/2019JB018513>.
- Long, T., Zhao, J.G., Liu, X.Z., Li, Z., Xiao, Z.J., Wang, Z.Z., Ouyang, F., 2020. Cross-band rock physics measurement and theoretical modeling of carbonate rocks—Study on the effect of different pore structure on the dispersion and attenuation of carbonate rocks. *Chin. J. Geophys.* 63, 4502–4516. <https://doi.org/10.6038/cjg202000234> (in Chinese).
- Lozovyi, S., Bauer, A., 2019. From static to dynamic stiffness of shale: frequency and stress dependence. *Rock Mech. Rock Eng.* 52, 5085–5098. <https://doi.org/10.1007/s00603-019-01934-1>.
- Madonna, C., Tisato, N., 2013. A new Seismic Wave Attenuation Module to experimentally measure low-frequency attenuation in extensional mode. *Geophys. Prospect.* 61, 302–314. <https://doi.org/10.1111/1365-2478.12015>.
- Mikhailovitch, V., Lebedev, M., Gurevich, B., 2014. A laboratory study of low-frequency wave dispersion and attenuation in water-saturated sandstones. *Lead. Edge* 43, 616–622. <https://doi.org/10.1190/le33060616.1>.
- Mikhailovitch, V., Lebedev, M., Gurevich, B., 2016a. Laboratory measurements of the effect of fluid saturation on elastic properties of carbonates at seismic frequencies. *Geophys. Prospect.* 64, 799–809. <https://doi.org/10.1111/1365-2478.12404>.
- Mikhailovitch, V., Lebedev, M., Gurevich, B., 2016b. Validation of the laboratory measurements at seismic frequencies using the Kramers-Kronig relationship: Kramers-Kronig relation for validation. *Geophys. Res. Lett.* 43, 4986–4991. <https://doi.org/10.1002/2016GL069269>.
- Müller, C., Gurevich, B., Lebedev, M., 2010. Seismic wave attenuation and dispersion resulting from wave-induced flow in porous rocks – a review. *Geophysics* 75, 75A147–75A164. <https://doi.org/10.1190/1.3463417>.
- Müller, C., Gurevich, B., 2004. One-dimensional random patchy saturation model for velocity and attenuation in porous rocks. *Geophysics* 69 (5), 1166–1172. <https://doi.org/10.1190/1.1801934>.
- Nowick, A.S., Bery, B.S., 1972. *Anelastic Relaxation in Crystalline Solids*. Academic press. <https://doi.org/10.1002/pol.1973.130110713>.
- O'Connell, R.J., Budiansky, B., 1978. Measurements of dissipation in viscoelastic media. *Geophys. Res. Lett.* 5, 5–8. <https://doi.org/10.1029/g1005i001p00005>.
- Pimienta, L., Fortin, J., Guéguen, Y., 2015. Experimental study of Young's modulus dispersion and attenuation in fully saturated sandstone. *Geophysics* 80, L57–L72. <https://doi.org/10.1190/geo2014-0532.1>.
- Pimienta, L., Fortin, J., Guéguen, Y., 2016. Effect of fluids and frequencies on Poisson's ratio of sandstone sample. *Geophysics* 81, D183–D195. <https://doi.org/10.1190/geo2015-0310.1>.
- Rubino, J.G., Holliger, K., 2013. Research note: seismic attenuation due to wave-induced fluid flow at microscopic and mesoscopic scales. *Geophys. Prospect.* 61, 882–889. <https://doi.org/10.1111/1365-2478.12009>.
- Spencer, J.W., 1981. Stress relaxation at low frequencies in fluid-saturated rocks: attenuation and modulus dispersion. *J. Geophys. Res.* 86, 1803–1812. <https://doi.org/10.1051/jphyscol:19815182>.
- Spencer, J.W., Shine, J., 2016. Seismic wave attenuation and modulus dispersion in sandstones. *Geophysics* 81, D211–D231. <https://doi.org/10.1190/geo2015-0342.1>.
- Subramaniyan, S., Quintal, B., Madonna, C., Saenger, E.H., 2015. Laboratory-based seismic attenuation in Fontainebleau sandstone: evidence of squirt flow. *J. Geophys. Res. Solid Earth* 120, 7526–7535. <https://doi.org/10.1002/2015JB012290>.
- Subramaniyan, S., Quintal, B., Tisato, N., Saenger, E.H., Madonna, C., 2014. An overview of laboratory apparatuses to measure seismic attenuation in reservoir rocks. *Geophys. Prospect.* 62, 1211–1223. <https://doi.org/10.1111/1365-2478.12171>.
- Sun, C., Tang, G.Y., Fortin, J., Borgomano, V.M., Wang, S.X., 2020. Dispersion and attenuation of elastic wave velocities: impact of microstructure heterogeneity and local measurements. *J. Geophys. Res. Solid Earth* 125 (12), 2020JB020132. <https://doi.org/10.1029/2020JB020132>.
- Sun, C., Tang, G.Y., Zhao, J.G., Zhao, L.M., Wang, S.X., 2018. An enhanced broad-frequency apparatus for dynamic measurement of elastic moduli and Poisson's ratio of rock samples. *Rev. Sci. Instrum.* 89, 064503. <https://doi.org/10.1063/1.5018152>.
- Szewczyk, D., Bauer, A., Holt, R.M., 2016. A new laboratory apparatus for the measurement of seismic dispersion under deviatoric stress conditions. *Geophys. Prospect.* 64, 789–798. <https://doi.org/10.1111/1365-2478.12425>.
- Tisato, N., Madonna, C., 2012. Attenuation at low seismic frequencies in partially saturated rocks: measurements and description of a new apparatus. *J. Appl. Geophys.* 86, 44–53. <https://doi.org/10.1016/j.jappgeo.2012.07.008>.
- Toms, J., Müller, T., Gurevich, B., 2007. Seismic attenuation in porous rocks with random patchy saturation. *Geophys. Prospect.* 55 (5), 671–678. <https://doi.org/10.1111/j.1365-2478.2007.00644.x>.
- Wang, S.X., Zhao, J.G., Li, Z., Harris, J.M., Quan, Y., 2012. Differential acoustic resonance spectroscopy for the acoustic measurement of small and irregular sample in the low frequency range. *J. Geophys. Res. Solid Earth* 117, B06203. <https://doi.org/10.1029/2011JB008808>.
- White, J.E., 1975. Computed seismic speeds and attenuation rocks with partial gas saturation. *Geophysics* 40 (2), 224–232. <https://doi.org/10.1190/1.1440520>.
- Winkler, K., Nur, A., 1979. Pore fluids and seismic attenuation in rocks. *J. Geophys. Res. Solid Earth* 90, 6793–6800. <https://doi.org/10.1029/GL006i001p00001>.
- Yin, H.J., Zhao, J.G., Tang, G.Y., Zhao, L.M., Ma, X.Y., Zhao, L.M., 2017. Pressure and fluid effect on frequency-dependent elastic moduli in fully saturated tight sandstone. *J. Geophys. Res. Solid Earth* 122, 8925–8942. <https://doi.org/10.1002/2017JB014244>.
- Zhao, J.G., Wang, S.X., Tong, X., Yin, H.J., Yuan, D., Ma, X., Deng, J.X., Xiong, B., 2015. Differential acoustic resonance spectroscopy: improved theory and application in the low frequency range. *Geophys. J. Int.* 202, 1775–1791. <https://doi.org/10.1093/gji/ggv234>.
- Zhao, L.M., Tang, G.Y., Wang, S.X., Zhao, J.G., Wang, X.M., Liu, H.J., Wei, G.H., Sun, C., Li, M.L., Li, M., 2019. Laboratory study of oil saturation and oil/water substitution effects on a sandstone's modulus dispersion and attenuation. *Explor. Geophys.* 50 (3), 324–335. <https://doi.org/10.1080/08123985.2019.1610327>.
- Zong, Z.Y., Chen, F.B., Yin, X.Y., Li, K., 2022. Effect of stress on wave propagation in fluid-saturated porous thermoelastic media. *Surv. Geophys.* 44 (2), 425–446. <https://doi.org/10.1007/s10712-022-09743-y>.